Physics of Plasmas

Lagrangian conditional statistics and flow topology in edge plasma turbulence

Cite as: Phys. Plasmas **29**, 102301 (2022); https://doi.org/10.1063/5.0098501
Submitted: 09 May 2022 • Accepted: 07 September 2022 • Published Online: 13 October 2022

Benjamin Kadoch, Diego del-Castillo-Negrete, Wouter J. T. Bos, et al.

Physics of Plasmas ARTICLE scitation.org/journal/php

Lagrangian conditional statistics and flow topology in edge plasma turbulence

Cite as: Phys. Plasmas **29**, 102301 (2022); doi: 10.1063/5.0098501
Submitted: 9 May 2022 · Accepted: 7 September 2022 ·
Published Online: 13 October 2022

Benjamin Kadoch,[1] Diego del-Castillo-Negrete,[2] Wouter J. T. Bos,[3] and Kai Schneider[4,a)]

AFFILIATIONS

[1]Aix-Marseille Université, CNRS, IUSTI, 13453 Marseille, France
[2]Oak Ridge National Laboratory, Oak Ridge, Tennessee 37831-6304, USA
[3]LMFA-CNRS, Ecole Centrale de Lyon, 69340 Ecully, France
[4]Aix-Marseille Université, CNRS, I2M, 13453 Marseille, France

[a)]Author to whom correspondence should be addressed: kai.schneider@univ-amu.fr

ABSTRACT

Lagrangian statistics and particle transport in edge plasma turbulence are investigated using the Hasegawa–Wakatani model and its modified version. The latter shows the emergence of pronounced zonal flows. Different values of the adiabaticity parameter are considered. The main goal is to characterize the role of coherent structures, i.e., vortices and zonal flows, and their impact on the Lagrangian statistics of particles. Computationally intensive long time simulations following ensembles of test particles over hundreds of eddy turnover times are considered in statistically stationary turbulent flows. The flow topology is characterized using the Lagrangian Okubo–Weiss criterion in order to split the flow into topologically different domains. In elliptic and hyperbolic regions, the probability density functions (PDFs) of the residence time have self-similar algebraic decaying tails. However, in the intermediate regions, the PDFs exhibit exponentially decaying tails. Topologically conditioned PDFs of the Lagrangian velocity, and acceleration and density fluctuations are likewise computed. The differences between the classical Hasegawa–Wakatani system and its modified version are assessed, and the role of zonal flows is highlighted. The density flux spectrum, which characterizes the contributions of different length scales, is studied, and its inertial scaling is found to be in agreement with predictions based on dimensional arguments. Analyzing the angular change of particle tracers at different time scales, corresponding to coarse grained curvature, completes the study, and these multiscale geometric statistics quantify the directional properties of the particle motion in different flow regimes.

I. INTRODUCTION

Drift-wave turbulence and zonal flows in the tokamak edge crucially determine the dynamics of magnetically confined plasma flow, its confinement properties, and non-diffusive transport. In recent years, there has been a significant interest in understanding this problem from a Lagrangian perspective. In this approach, transport properties of the system are studied by tracking the trajectories of large ensembles of tracers. In numerical simulations, this is accomplished by solving the equations for the trajectories of test particles in a given velocity field, e.g., the $\boldsymbol{E} \times \boldsymbol{B}$ velocity field in the guiding center description of a plasma. One of the main lessons learned from the Lagrangian approach is that coherent structures have a profound influence on transport. In particular, the combined effect of the trapping by eddies and the long displacements induced by zonal shear flows typically gives rise to non-diffusive transport.[1–3] From the Lagrangian point of view, non-diffusive transport is characterized by the anomalous scaling of the statistical moments of the particle's displacements $\langle \delta x^2 \rangle \sim t^{\gamma}$, where δx denotes the particle's displacements, t denotes the time, $0 < \gamma < 2$, and $\langle\,\rangle$ denotes the ensemble average. In the case of diffusive transport, $\gamma = 1$, whereas for non-diffusive transport $\gamma \neq 1$.

It has been experimentally and numerically observed that edge turbulence typically develops coherent structures, e.g., blobs, streamers, and shear flows; see, for example, Ref. 1 and references therein. The understanding of the role of these coherent structures on the particle and heat transport is a critical step to guaranteeing the confinement needed in a fusion reactor. However, establishing a quantitative connection between coherent structures (e.g., vortices and zonal flow) and transport, and in particular, anomalous diffusion (e.g., sub-diffusion and superdiffusion), can be a highly nontrivial task. Studies based on simple transport models [e.g., chaotic advection models (see, for example, Ref. 4)] and on generalized random

walk models (e.g., continuous time random walks) have shown that typically, when the trapping effects of eddys dominate, $\gamma < 1$, and transport is sub-diffusive (i.e., slower than diffusion). However, when zonal flows dominate, transport along the zonal flow becomes highly anisotropic while radial transport essentially vanishes. Although in fusion plasmas radial transport is the main concern, poloidal transport is also of interest. Beyond fusion plasmas, transport in the direction of the zonal flow is a problem of significant interest in geophysical flows, e.g., the Gulf Stream. However, establishing this connection at a quantitative level has proved elusive in the case of flows with complex spatiotemporal structures (e.g., turbulent plasmas and fluids), because in these systems, the coherent structures typically exhibit complicate dynamics. For example, in 2D turbulence, the size and location of trapping regions changes unpredictably in space and time due to vortex merging and decay. In the case of bounded flows, boundary layers create intense vorticity dominated regions near the walls that might temporally trap particles. Moreover, a particle that is "trapped" in an eddy will not necessarily be confined to a region in space since the eddy might be moving throughout the whole domain. Further complications appear in systems that exhibit rapid transport phenomena that give rise to intermittent large particle displacements. This type of phenomena, sometimes referred to as "avalanche-like" transport, is routinely observed in plasma turbulence models near marginal stability. In this case, tracers are transported over large distances by short-lived coherent structures.

The key question then is, given a Lagrangian trajectory of a tracer, $\boldsymbol{x}(t)$, in a flow with a complex spatiotemporal dynamics, how can we characterize the signatures of trapping due to eddies and long-displacements (flights), from the information contained in the trajectory? The answer to this question is important, because it is the first step to characterize the statistics of trapping and flights in turbulent transport. This statistics is the cornerstone in the construction of effective models for nondiffusive transport in the context of the continuous time random walk model and in fractional diffusion, see, for example, Refs. 2 and 3.

In Ref. 5, the authors showed for the large plasma device (LAPD) that turbulence fluctuations have non-Gaussian characteristics, while the radial flux of plasma density is similar to Bohm diffusion. The latter is not valid in large tokamaks where zonal flows suppress transport. Garland *et al.*[6] presented a study investigating the influence of collisionality on intermittency in drift-wave turbulence using both numerical and experimental approaches, the latter for the TJ-K stellerator; they showed an increase in intermittency with increasing collisionality for density fluctuations. The study in Ref. 7 revealed the importance of considering local magnetic curvature properties as a factor in the decoupling of density and potential fluctuations leading to intermittency in drift-wave turbulence.

As mentioned before, when the coherent structures are time independent and fixed in space, the answer to this question is simple: trapping (flight) events correspond to sections of the trajectory for which $\boldsymbol{x}(t)$ is contained in an eddy (shear flow). For general flows, Ref. 8 proposed a simple characterization based on the intuition that the radial component of the Lagrangian velocity would stay small (and varying sign rapidly) while trapped and become large (with a well-defined sign) during a flight event. This idea was implemented in Ref. 9 to study the non-Gaussian statistics of trapping and flight events in near-critical dissipative-trapped-electron-mode turbulence. Reference 10 proposed a definition of trapping based on the time that nearby particles stay close to study anomalous diffusion and exit time statistics of tracers in a fluid model of resistive pressure-gradient-driven plasma turbulence. In the study of mesoscale transport in near critical resistive pressure-gradient-driven turbulence in toroidal geometry presented in Ref. 11, a flight was defined as the portion of the trajectory that keeps the same sign in the radial velocity. Despite the fact that these studies provided valuable insight into the nature of nondiffusive transport in plasma turbulence, there is a need to provide a more conclusive, systematic, and quantitative measure of trapping and flight events from a Lagrangian perspective. As a first step to address this important challenging problem, in this paper, we propose a method to characterize the Lagrangian statistics of tracers based on the topological properties of the turbulence. Based on a previous work in Ref. 12, we characterize the topology of a flow using the Okubo–Weiss criterion, which provides a conceptually simple tool to partition a flow into topologically different regions: elliptic (vortex dominated), hyperbolic (deformation dominated), and intermediate (turbulent background). A quantity of interest to be considered is the curvature of particle trajectories, which is directly related to Lagrangian acceleration and characterizes their intermittency.[13] However, different from Ref. 12, which was limited to Navier–Stokes fluid turbulence, we consider the Hasegawa–Wakatani (HW) system that provides one of the simplest models to study cross field transport by electrostatic drift waves in magnetically confined plasmas, in general, and in the plasma edge, in particular. More precisely, the HW model describes 2D drift-wave turbulence in a collision dominated plasma in a slab geometry and is valid in the confined steep-gradient region just inside the last closed flux surface.[14] In this model, some aspects of the strong $E \times B$ shear pedestal flow can be captured by the poloidal zonal flow observed in the modified version of the HW model. For a detailed discussion, one can refer to Ref. 15.

In addition to the classical Hasegawa–Wakatani model, we consider a modified version proposed in Ref. 16. and used in Ref. 17. This modified version exhibits pronounced zonal flows for large adiabaticity values, and the flow characteristics differ significantly from those obtained in the classical version of the model.

As a second step, geometric statistics of the particle trajectories are performed by analyzing the angular change of particle tracers at different time scales. The thus obtained angular curvature angle corresponding to coarse grained curvature of the trajectories quantifies the directional properties of the complex particle motion in different flow regimes from a Lagrangian perspective. The directional change of a particle is then directly related to the coarse grained curvature. It yields a timescale dependent measure and can characterize the time correlation of the direction of a particle in a turbulent flow. Thus, the multiscale characteristic of turbulence can be revealed from a Lagrangian perspective and is related to the topology of the Lagrangian trajectories, see Ref. 13. To avoid confusion, the Lagrangian curvature considered in this study is understood in the sense of the trajectory curvature and must not be confused with the magnetic curvature. One can also note that there is a possible link with the recently introduced longitudinal and transversal Lagrangian structure functions.[18]

The remainder of the manuscript describes the Hasegawa–Wakatani turbulence model in Sec. II and recalls the Okubo–Weiss criterion used to partition the flow into distinct regions. Tools for performing directional Lagrangian statistics, including the coarse-grained

curvature angle, are likewise introduced in Sec. II. Results on Eulerian statistics and Lagrangian conditional statistics for different flow regimes are presented and discussed in Sec. III. Finally, we conclude and give some perspectives for future work in Sec. IV.

II. EDGE TURBULENCE MODEL

As a numerically tractable model for edge turbulence, we consider the Hasegawa–Wakatani turbulence model describing the drift wave-zonal flow interaction in a two-field coupled system in a shearless slab geometry.[19] A sketch illustrating the flow configuration, considering a two-dimensional slab in the radial-poloidal plane, is given in Fig. 1.

A. Eulerian description

The closed set of equations, describing the evolution of vorticity $\omega = \nabla^2\phi$ of the $E \times B$ motion (with ϕ being the electrostatic potential) and of the plasma density fluctuations n, reads

$$\left(\frac{\partial}{\partial t} - \nu\nabla^2\right)\nabla^2\phi = \left[\nabla^2\phi, \phi\right] + c(\phi - n), \tag{1}$$

$$\left(\frac{\partial}{\partial t} - D\nabla^2\right)n = [n, \phi] - \boldsymbol{u}\cdot\nabla\ln\left(\langle n\rangle\right) + c(\phi - n). \tag{2}$$

All quantities are dimensionless and have been suitably normalized, as described in Refs. 20 and 21. The coordinates x and y denote the radial and poloidal directions, respectively. The constant parameters D and ν are, respectively, the cross field diffusion of the plasma density fluctuations n and the kinematic viscosity. The adiabaticity c is given by

$$c = \frac{T_e k_z^2}{e^2 n_0 \eta \omega_{ci}}, \tag{3}$$

with T_e being the electron-temperature, k_z the effective parallel wavenumber (i.e., parallel to the magnetic field), e the electron charge, n_0 the reference plasma density, η the electron resistivity, and ω_{ci} the ion-gyro-frequency. The Poisson brackets are defined as $[a, b] = \frac{\partial a}{\partial x}\frac{\partial b}{\partial y} - \frac{\partial a}{\partial y}\frac{\partial b}{\partial x}$. The mean plasma density $\langle n\rangle$ acts as a source driving the density fluctuation dynamics. In particular, for a profile of the form $\langle n\rangle = n_0(x) = N_0\exp(-x/L_n)$, where N_0 is a constant number density and L_n is a characteristic length scale for the density gradient, the second term on the right-hand side of Eq. (2) reduces to $-\Gamma u_x$, where $\Gamma = (N_0/L_n)$ is the mean density gradient. The electrostatic potential ϕ plays for the $E\times B$ velocity the role of a stream-function, $\boldsymbol{u} = \nabla^\perp\phi$, where $\nabla^\perp = (-\partial_y, \partial_x)$, i.e., we have $u_x = -\partial\phi/\partial y$ and $u_y = \partial\phi/\partial x$. The coupling term $c(n-\phi)$, present in both equations, is related to the parallel current density and triggers the electrostatic plasma instability. The adiabaticity value c, which quantifies the collisionality of ions and electrons, determines the dynamics. Large collisionality corresponding to small c values coincides with the hydrodynamic 2D limit characterized by the presence of long living coherent vortices in the $\boldsymbol{E}\times\boldsymbol{B}$ flow and almost passive advection of the density fluctuations. Intermediate values of c of order unity yield dynamics, which are supposed to be close to tokamak edge-turbulence, the so-called quasi-adiabatic regime. In the limit $c\to\infty$, we obtain the Hasegawa–Mima model,[22] which corresponds to the Charney equation for Rossby waves used for modeling geophysical flows, also known as a geostrophic regime. Note that geometrical variations of the magnetic field can be neglected as the domain is chosen sufficiently small, i.e., of size 64 ρ_s, where ρ_s is the Larmor radius. The magnetic field lines of the unperturbed constant magnetic field are straight, and they are assumed to be perpendicular to the slab. In addition to the classical Hasegawa–Wakatani model (cHW), described above, we also consider a revised version, named modified Hasegawa–Wakatani model (mHW), which was introduced in Ref. 16. To obtain zonal flows for large adiabaticity values, $k_y = 0$ modes of the coupling term $[c(\phi - n)]$ are set to zero in mHW, similarly to what has been done in Ref. 17.

The Lagrangian acceleration of tracer particles $\boldsymbol{a}_L$, advected by the $E\times B$ velocity can be defined in the Eulerian reference frame using the momentum evolution equation

$$\boldsymbol{a}_L = \frac{\partial\nabla^\perp\phi}{\partial t} + \left[\phi, \nabla^\perp\phi\right] = -\nabla p + \nu\nabla^2\boldsymbol{u} - \frac{\nabla^\perp}{\nabla^2}\left[c(n-\phi)\right], \tag{4}$$

where p denotes pressure and $\nabla^\perp/\nabla^2$ denotes the Biot–Savart operator.

Equations (1) and (2) are solved numerically in a double-periodic domain of size 64^2. To this end, a fully dealiased pseudo-spectral method with a resolution of 1024^2 grid points is used. The time step is 5×10^{-4} and for the diffusivity of the plasma density and the kinematic viscosity we use $D = 5\times10^{-3}$ and $\nu = 5\times10^{-3}$, respectively. This results in a Schmidt number of unity ($Sc = \nu/D = 1$). The value of Γ in the mean density gradient of plasma density fluctuations is equal to one, i.e., $\Gamma = 1$.

The simulations are initialized with Gaussian random initial conditions and run until a saturated, fully developed turbulent flow is obtained. This transition phase is typically quite time consuming and may take millions of time steps. Subsequently, 10^4 particles were uniformly injected, and their velocity and acceleration were monitored during a large number of large-scale turn-over times (Table I). The eddy turn-over time t_k is defined as $1/\sqrt{2Z_{rms}}$, where Z_{rms} is the RMS vorticity. It is of the same order of magnitude in the different regimes, $\sim$0.5 for $c \le 2$ for classical Hasegawa–Wakatani (cHW) and $\sim$1 for modified Hasegawa–Wakatani (mHW). The adiabaticity is varied between $c = 0.01$ and 4 to obtain different flow regimes. Series of long time simulations have been performed for both cHW and mHW. Compared to the simulations in Ref. 17 we use instead of hyperviscosity classical Newtonian viscosity. Qualitatively, the results are similar,

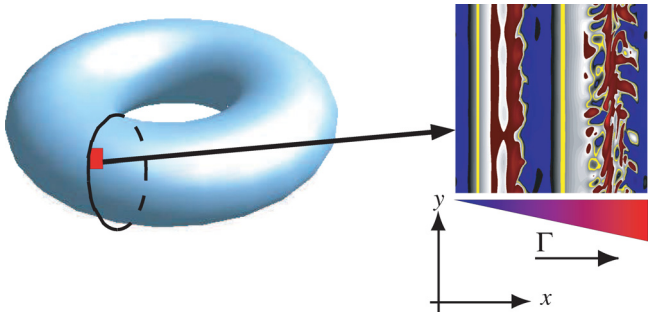

FIG. 1. Sketch of the flow configuration in the 2D slab geometry in the tokamak edge modeled by the Hasegawa–Wakatani system, where x denotes the radial direction and y the poloidal direction. A mean plasma density gradient in the radial direction Γ is imposed, and the 2D flow in the domain of size 64 ρ_s is computed, where ρ_s is the Larmor radius. The computational domain is illustrated by the red square. A snapshot of the vorticity field for modified Hasegawa–Wakatani (mHW) with zonal flows is shown on the right.

TABLE I. Physical parameters of the cHW and mHW simulations, where c denotes the adiabaticity. Root mean squares of the total energy and enstrophy are denoted, respectively, by E_{rms} and Z_{rms}. The Reynolds number R_λ is based on the Taylor microscale λ, and ν denotes the kinematic viscosity. The mean eddy turn over time is denoted by t_k and the time interval where the statistical analyses were done by t_d, corresponding in all cases to about 150 t_k.

Configurations	$\lambda = \frac{\sqrt{E_{rms}}}{Z_{rms}}$	$R_\lambda = \lambda \frac{\sqrt{E_{rms}}}{\nu}$	$t_k = \frac{1}{\sqrt{2Z_{rms}}}$	$\frac{t_d}{t_k}$
$c = 0.01$ cHW	1.53	679	0.49	307
$c = 0.05$ cHW	1.09	432	0.39	388
$c = 0.10$ *cHW*	0.95	341	0.37	404
$c = 0.70$ cHW	0.74	218	0.35	427
$c = 2.00$ cHW	0.82	225	0.42	354
$c = 4.00$ cHW	1.13	283	0.64	234
$c = 2.00$ mHW	3.27	380	3.96	38
$c = 4.00$ mHW	3.14	345	4.03	37

which show that the dynamics does not critically depend on the choice of the small scale damping.

B. Lagrangian description: Trajectories, curvature, and coarse-grained curvature

Considering passive tracer particles in drift-wave turbulence is motivated by analyzing, for instance, the transport of impurities in the plasma edge. In the Lagrangian setting, the time evolution of a tracer particle position $\boldsymbol{x}(t)$ obeys to the classical differential equation

$$\frac{d\boldsymbol{x}}{dt} = \boldsymbol{u}(\boldsymbol{x}(t), t), \tag{5}$$

completed with the initial position of the tracer particle $\boldsymbol{x}(t = 0) = \boldsymbol{x}_0$. The velocity $\boldsymbol{u}$ is obtained at the particle position $\boldsymbol{x}(t)$ using bicubic interpolation from the velocity field, and the time advancement of particles is done using a second-order Runge–Kutta scheme with time step 5×10^{-4}. The curvature κ of the particle trajectory $\boldsymbol{x}(t)$ is also considered in this study, in particular, for analyzing Lagrangian intermittency[12] and defined by

$$\kappa = \frac{a_n}{||\boldsymbol{u}_L||^2}, \tag{6}$$

where a_n is the component of the Lagrangian acceleration, in Eq. (4), normal to the velocity vector. The curvature vanishes when the particle velocity and the acceleration vectors are parallel, and we can note that $\kappa \geq 0$. All the Lagrangian statistics are computed using ensemble and time averages (with the exception of the residence time where only ensemble averaging is applied), and the subscript L is used to denote Lagrangian quantities. Further details on the simulations using Eqs. (1) and (2) can be found in Ref. 20. For the Lagrangian part of the study, we refer to Ref. 23, where a similar investigation was performed for Navier–Stokes turbulence.

To get insight into the complex multiscale dynamics of drift-wave turbulence and zonal flows from a Lagrangian perspective, we quantify directional motion in stochastic trajectories statistically at different time scales using the curvature angle.[13,24] To determine this directional change, the angle between subsequent particle displacement increments is evaluated as a function of the timelag, and, thus, multi-scale geometric statistics can be performed. We define the Lagrangian spatial increment as $\delta\boldsymbol{X}(\boldsymbol{x}_0, t, \tau) = \boldsymbol{x}(t) - \boldsymbol{x}(t - \tau)$, where $\boldsymbol{x}(t)$ is the position of a fluid particle at time t, passing through point $\boldsymbol{x}_0$ at the reference time $t = t_0$ and advected by a velocity field $\boldsymbol{u}$, Eq. (5), as illustrated in Fig. 2. The cosine of the angle $\Theta(t, \tau)$ between subsequent particle increments, introduced in Ref. 24 and analyzed in three-dimensional homogeneous isotropic turbulence[13] and in two-dimensional homogeneous isotropic and confined turbulence,[25] is

$$\cos(\Theta(t, \tau)) = \frac{\delta\boldsymbol{X}(\boldsymbol{x}_0, t, \tau) \cdot \delta\boldsymbol{X}(\boldsymbol{x}_0, t + \tau, \tau)}{|\delta\boldsymbol{X}(\boldsymbol{x}_0, t, \tau)|\,|\delta\boldsymbol{X}(\boldsymbol{x}_0, t + \tau, \tau)|}. \tag{7}$$

The curvature angle Θ can be related to the curvature κ introduced in Eq. (6). In the limit when τ goes to zero, the curvature angle yields the curvature κ, as discussed in Refs. 13 and 26. For finite values of τ, we obtain a finite time curvature measure $K(t, \tau)$, corresponding to a coarse grained curvature and the influence of τ can be analyzed. To this end, the scale-dependent curvature angle must be properly normalized, i.e., dividing $\Theta(t, \tau)$ by $2\tau||\boldsymbol{u}||$, and thus, we obtain $K(t, \tau) = \Theta(\tau)/(2\tau||\boldsymbol{u}||)$.

C. Lagrangian flow topology

The Okubo–Weiss criterion[27,28] is a well-established tool to characterize the topology of turbulent flow fields. Hereby, the flow field can be partitioned into topologically distinct regions, i.e., into vorticity dominated regions, which correspond to elliptic zones, strong deformation regions which correspond to hyperbolic zones and likewise into intermediate regions. At a given time instant, the flow parameter Q, also called the Weiss value, is determined as

$$Q = s^2 - \omega^2, \tag{8}$$

where $\omega = \partial_x u_y - \partial_y u_x$ is the vorticity and $s^2 = s_1^2 + s_2^2$ is the deformation with

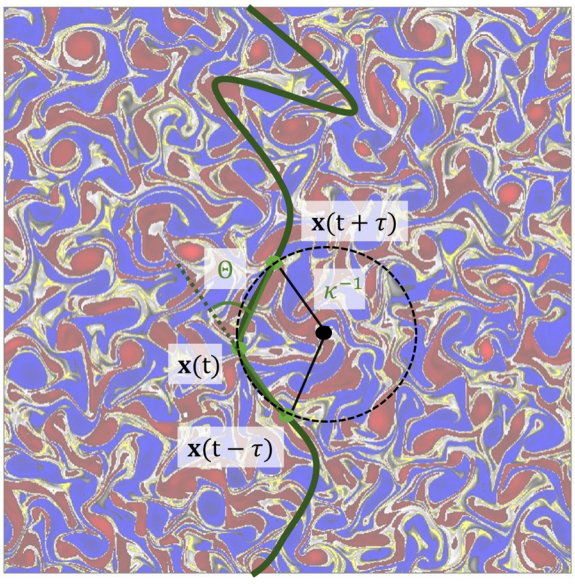

FIG. 2. Sketch of the coarse-grained curvature angle Θ and the curvature κ. A sample trajectory is superimposed to a vorticity field. Three trajectory positions $\boldsymbol{x}(t)$ at three time instants, $t - \tau, t$, and $t + \tau$ are marked by green dots and used to determine the curvature angle Θ.

$$s_1 = \frac{\partial u_x}{\partial x} - \frac{\partial u_y}{\partial y}, \quad s_2 = \frac{\partial u_y}{\partial x} + \frac{\partial u_x}{\partial y}. \tag{9}$$

Then using the local value of Q, the flow domain can be partitioned in three disjoint regions, as suggested, for instance, in Ref. 12:

(i) strongly elliptic for which $Q \leq -Q_0$ (vorticity dominated),
(ii) strongly hyperbolic for which $Q \geq Q_0$ (deformation dominated),
(iii) intermediate regions for which $-Q_0 < Q < Q_0$.

The threshold value Q_0 can be chosen, for instance, as the standard deviation of Q, i.e., $Q_0 = \sqrt{\langle Q^2 \rangle}$, where $\langle \cdot \rangle$ is the ensemble average. The space-time-dependent function, given in Eq. (8), $Q(\boldsymbol{x}, t)$ is the Eulerian definition of the Weiss field. Alternatively, given a trajectory $\boldsymbol{x}(t)$ obtained from the solution of Eq. (5), the Lagrangian Weiss field is defined as the time-dependent function $Q_L(t) = Q(\boldsymbol{x}(t))$, i.e., the value of Q along the particle trajectory. Motivated by conditional Lagrangian statistics, we focused in this study on the Lagrangian Weiss field, a technique we introduced in Ref. 12. To this end, the Weiss field is considered along individual particle trajectories rather than as a function of the spatial coordinates in the flow. Classically, the Okubo–Weiss criterion is applied in an Eulerian framework only and comes with a theoretical justification. The Okubo–Weiss criterion is based on the linearization of the Navier–Stokes equation and the assumption that the strain field remains frozen. Some of its limitations are discussed in Ref. 29.

Based on this partitioning of the flow, the residence time can be considered for different regions. The time during which a particle remains in the same zone (strong elliptic, strong hyperbolic, or intermediate regions) can be determined.

III. RESULTS

A. Flow topology and Eulerian statistics

A series of six simulations has been performed for the classical Hasegawa–Wakatani system and two simulations have been conducted for the modified system. Table I summarizes the physical parameters of the eight configurations. Different values of the adiabaticity are considered ranging from 0.01, corresponding to a hydrodynamic regime, via 0.7 relevant for edge turbulence in fusion plasmas and called a quasi-adiabatic regime, up to values of 4.0, which yields a geostrophic regime and is similar to Hasegawa–Mima flows. For the two modified cases mHW, we consider $c = 2$ and $c = 4$ with the motivation to obtain zonal flows.

After a transient, exhibiting drift-wave instabilities, all configurations reach a statistically steady regime, see Appendix. The present study focuses on the statistically steady state obtained for different cases.

The Eulerian spectrum of kinetic energy is defined as

$$E_{kin}(k, t) = \frac{1}{2} \int_{\Sigma(k)} \mathcal{F}|_{x-x'} \left[\overline{\boldsymbol{u}(\boldsymbol{x}, t) \cdot \boldsymbol{u}(\boldsymbol{x}', t)} \right] d\Sigma(k), \tag{10}$$

where $\mathcal{F}$ denotes the 2D Fourier transform with respect to the separation vector $\boldsymbol{x} - \boldsymbol{x}'$ and $\Sigma(k)$ is the circular wavenumber shell of radius k. The spectrum of density fluctuations $E_n(k, t)$ is defined correspondingly, replacing $\boldsymbol{u} \times n$. The kinetic energy spectrum in Fig. 3 (top left) quantifies the contribution of the different length scales (or wavenumbers) and exhibits a k^{-4} power law behavior for all considered cHW cases. This is consistent with previous works, see, e.g., Ref. 30. The two mHW cases yield likewise clear power laws; however, the slope is steeper and found to be close to –6. For the spectra of the density fluctuations also power laws can be observed (Fig. 3 top right), but their slopes differ and vary from -2 in the hydrodynamic case (which is different from the classical Batchelor scaling corresponding to -1) to steeper spectral slopes for higher values of c. For cHW, this is consistent with what is found in Ref. 5 for large azimuthal wavenumbers, i.e., a power law close to $\propto k^{-6}$ using the BOUT code.[31]

Similar to investigations on turbulent transport in incompressible Navier–Stokes turbulence in the presence of an imposed mean scalar gradient,[32–34] we now consider the mean density flux $\overline{u_x n}$, where u_x and n are the radial velocity fluctuations and the density fluctuations, respectively. The mean scalar flux term (here, the mean density flux term) represents the influence of the turbulent fluctuations on the mean scalar profile (here the mean density profile) in the context of fluid turbulence. The importance of this term has been discussed in detail by Schiestel.[35] Note that for large collisionality, i.e., for small c values the density equation (2) corresponds indeed to a passive scalar equation with mean scalar gradient Γu_x. The mean flux contribution at the different length scales can be quantified considering the density flux spectrum, also known as co-spectrum in the literature, see e.g., Ref. 34 and references therein. Like the energy spectrum (10), it is defined by computing the Fourier transform of the correlation between u_x and n,

$$F_{u_x n}(k, t) = \frac{1}{2} Re \left[\int_{\Sigma(k)} \mathcal{F}|_{x-x'} \left[\overline{u_x(\boldsymbol{x}, t)\, n(\boldsymbol{x}', t)} \right] d\Sigma(k) \right]. \tag{11}$$

The co-spectrum $F_{u_x n}$ is real valued, and by construction, we have

$$\overline{u_x n} = \int_0^\infty F_{u_x n}(k)\, dk, \tag{12}$$

where the flux density $dF(k) = F_{u_x n}(k)\, dk$ quantifies the contributions of the mean density flux across different length scales (or wavenumbers).

Interestingly, the co-spectrum naturally connects the Eulerian and the Lagrangian flow description, as the density field yields some extent insight into the Lagrangian dynamics of the velocity field. The Lagrangian timescale relates the energy spectrum with the scalar flux spectrum[36] and, thus, provides a link between the scalar field and the Lagrangian dynamics of the turbulent velocity field. The Lagrangian spectral timescale $\tau(k)$ can be defined by

$$\tau(k) = \frac{\Gamma^{-1} |F_{u_x n}(k)|}{E_{kin}(k)}, \tag{13}$$

and dimensional analysis yields a spectrally local estimate

$$\tau(k) \propto \left[k^3 E_{kin}(k) \right]^{-1/2}, \tag{14}$$

which was proposed in Ref. 34. In our case, the scalar field corresponds to the density fluctuations, and the above results shall be valid at least in the limit of small c values in the cHW case. We, thus, obtain an estimation for the scaling of the density flux in the inertial range

$$F_{u_x n}(k) \propto \Gamma \sqrt{\frac{E_{kin}(k)}{k^3}}. \tag{15}$$

From a physical point of view, the timescale $\tau(k)$ corresponds to a correlation time. The decorrelation of turbulent scales in an inertial range

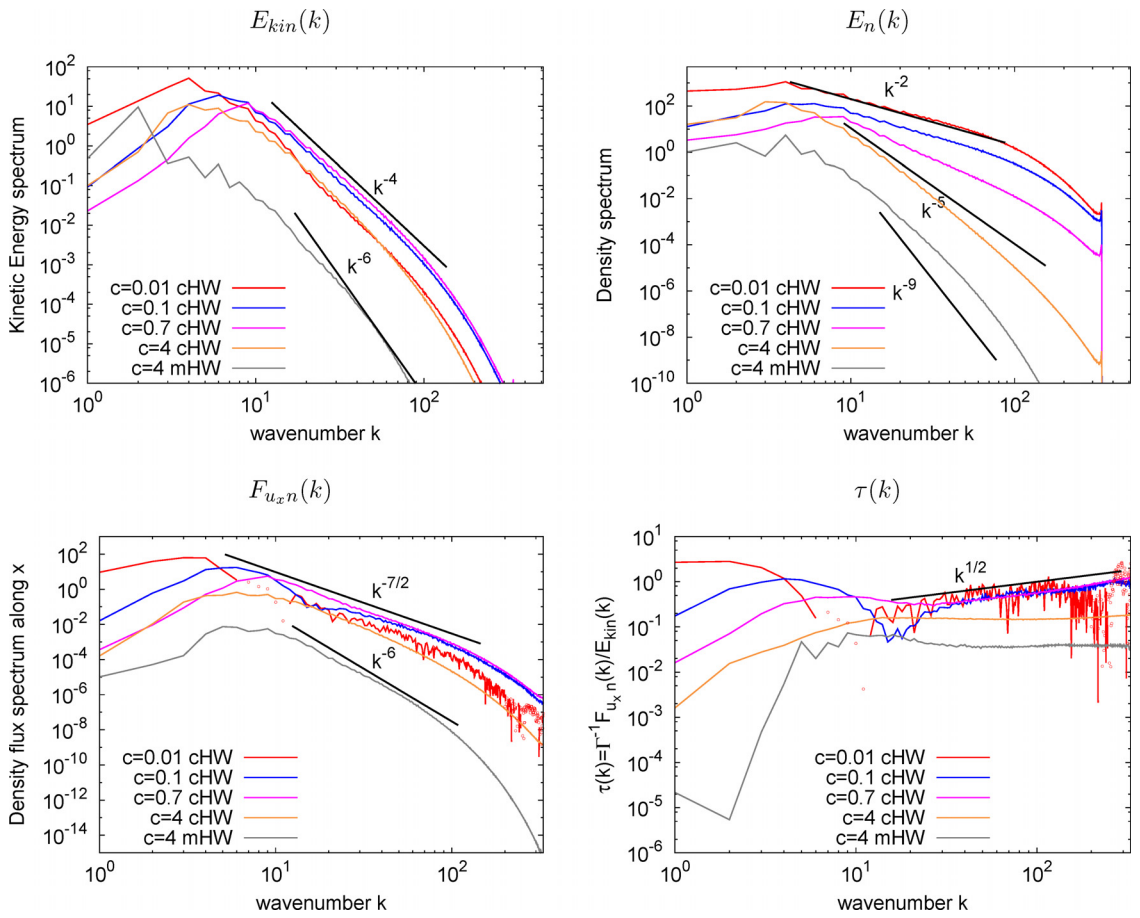

FIG. 3. Top: Eulerian kinetic spectra $E_{kin}(k)$ (left) and Eulerian spectra $E_n(k)$ of density fluctuations (right). Bottom: density flux spectra $F_{u_x n}(k)$ (left) and spectral timescale $\tau(k) = \Gamma^{-1}|F_{u_x n}(k)|/E_{kin}(k)$ (right). All the spectra are obtained using time-averaging with 75 snapshots taken at regular time intervals in the statistically stationary regimes. Dots in the spectra indicate negative values, plotted by taking the absolute value.

is generally due to straining or shearing. If we consider a *steep* kinetic energy distribution, this straining at a scale k is not only due to scales around k but may also be due to the interaction with all scales with wavenumbers smaller than k, cf. Ref. 37. Indeed, in 2D Navier–Stokes turbulence, the slope k^{-3} in energy spectra is the limit value between dynamics dominated by either local or non–local interactions. Only for spectra steeper than -3, one can show that nonlocal interactions[38] are dominant. Some discussion about nonlocal and local interactions on the intermittency corrections in three-dimensional turbulence can be also found in Laval *et al.*[39] So the slopes obtained in the energy spectra using the HW model, i.e., $n \geq 4$, are clearly indicators for non-local interactions at least at small scales. This interaction with small scales is taken into account by using instead of a spectrally local estimate, a "straining" time

$$\tau(k) \propto \left[\int_{k_0}^{k} p^2 E_{kin}(p)\, dp\right]^{-1/2}. \tag{16}$$

In particular, this time behaves qualitatively differently from the local timescale for kinetic energy spectra $E_{kin}(k) \propto k^{-n}$ for $n > 3$. Note that k_0 is a cutoff wavenumber to remove the infrared divergence. Using the dimensional analysis in Eq. (14), the timescale would satisfy $\tau(k) \sim k^{(n-3)/2}$, while the "straining" time estimate in Eq. (16) yields $\tau(k) \sim k^0$, valid for steep kinetic energy spectra. The latter implies also that the scalar flux spectrum and the kinetic energy spectrum satisfy the same scaling, $F_{u_x n}(k) \propto E_{kin}(k)$.

Inspecting Fig. 3 (bottom left) shows that for all cHW cases, we obtain a clear scaling behavior of $k^{-7/2}$ for the density flux spectrum as predicted in Eq. (15) with the observed k^{-4} scaling of the kinetic energy spectrum [Fig. 3 (top left)]. For $c = 0.7$, the relevant case for edge turbulence in fusion plasmas, this scaling is particularly well pronounced. The spectral timescale $\tau(k)$ shown in Fig. 3 (bottom right) exhibits the corresponding $k^{1/2}$ scaling, according to Eq. (14). Note that the rough estimation based on the Cauchy–Schwarz inequality and proposed by Smith *et al.*[40] yields $F_{u_x n}(k) \propto E_{kin}(k)^{1/2} E_n(k)^{1/2}$. It would, thus, predict slopes ranging from -3 to $-9/2$ for the cHW cases, which are clearly not found, as illustrated for 2D Navier–Stokes turbulence.[34] Further research is certainly required to understand why the constant behavior k^0 is found for $c = 4$ cHW. For mHW, we find a scaling of $F_{u_x n}(k) \propto k^{-6}$, which is steeper than the expected $-9/2$

slope and, thus, cannot be justified in Eq. (15). The corresponding spectral timescale $\tau(k)$ in Fig. 3 (bottom right) shows a constant behavior, i.e., a horizontal line for more than one decade and is, hence, independent of the wavenumber. This is in agreement with the "straining" timescale, defined in Eq. (16), the estimate for steep kinetic energy spectra. The observed k^{-6} scaling of the density flux spectra, i.e., we have $F_{u_x n}(k) \propto E_{kin}(k)$ can, therefore, be explained.

Now we consider higher order statistics and analyze the probability density functions (PDFs) of the different Eulerian quantities, which are computed using ensemble averaging. To this end, histograms of snapshots of the considered fields are computed using 100 bins. Subsequently, time-averaging with 75 snapshots taken at regular time intervals in the statistically stationary regime is applied. The PDFs of Eulerian vorticity, shown in Fig. 4 (left), exhibit a change in behavior with c. For the adiabatic regime ($c = 0.7$) and the case $c \geq 2$ cHW, the PDFs have an almost Gaussian shape. The PDFs of Eulerian density in Fig. 4 (right) appear to be Gaussian, except for the hydrodynamic regime where we can observe a small deviation from the parabolic shape for large positive and negative values. Concerning the modified case (cf. the second moment order for the corresponding Lagrangian quantities in Table II), the PDFs of density and vorticity show peaks at values different from zero, which can be attributed to the dominant contributions of the shearing zonal flows to the vorticity in these cases.

The PDFs of Eulerian density flux along x and y-directions are plotted in Fig. 4 (bottom). The PDFs are almost symmetric and exhibit heavy tails for $c = 0.01$. For larger values of c, an exponential behavior can be observed, and the variance (cf. Table II) decreases with increasing c and, thus, the range of values likewise shrinks. The difference is more significant for small adiabaticity values and almost insignificant for $c > 0.7$ (cHW). As a conclusion, the density fluxes have larger values and are more important for hydrodynamic regimes with extreme values much larger for $c = 0.01$. For the two mHW cases (cf. Table II), we observe strongly reduced density flux values, which again might be due to the presence of zonal flows.

The snapshots of vorticity, density, three-level Eulerian Weiss fields, and the density flux in the radial direction, in Fig. 5, illustrate the different flow regimes obtained by varying the adiabaticity. The snapshots are taken at a time, which is representative for a statistically stationary state. For low adiabaticity, $c = 0.01$, the flow regime is close to the ones obtained in hydrodynamic turbulence. The simulations for large c values are computationally very demanding due to a long transient phase (cf. Appendix). Zonal flows occur periodically after subsequent destabilization by shear flows. The flow visualizations in Fig. 5, i.e., vorticity, density, three-level Eulerian Weiss fields, and the density flux in the radial direction also include some sample trajectories. We observe that the flow structures in the vorticity field change with c and in the mHW case, we observe pronounced zonal flows in the poloidal direction. This change of behavior can be likewise found in the corresponding density and density flux fields. In the Weiss fields, we can see that elliptic regions dominate the flow fluid for low adiabaticity

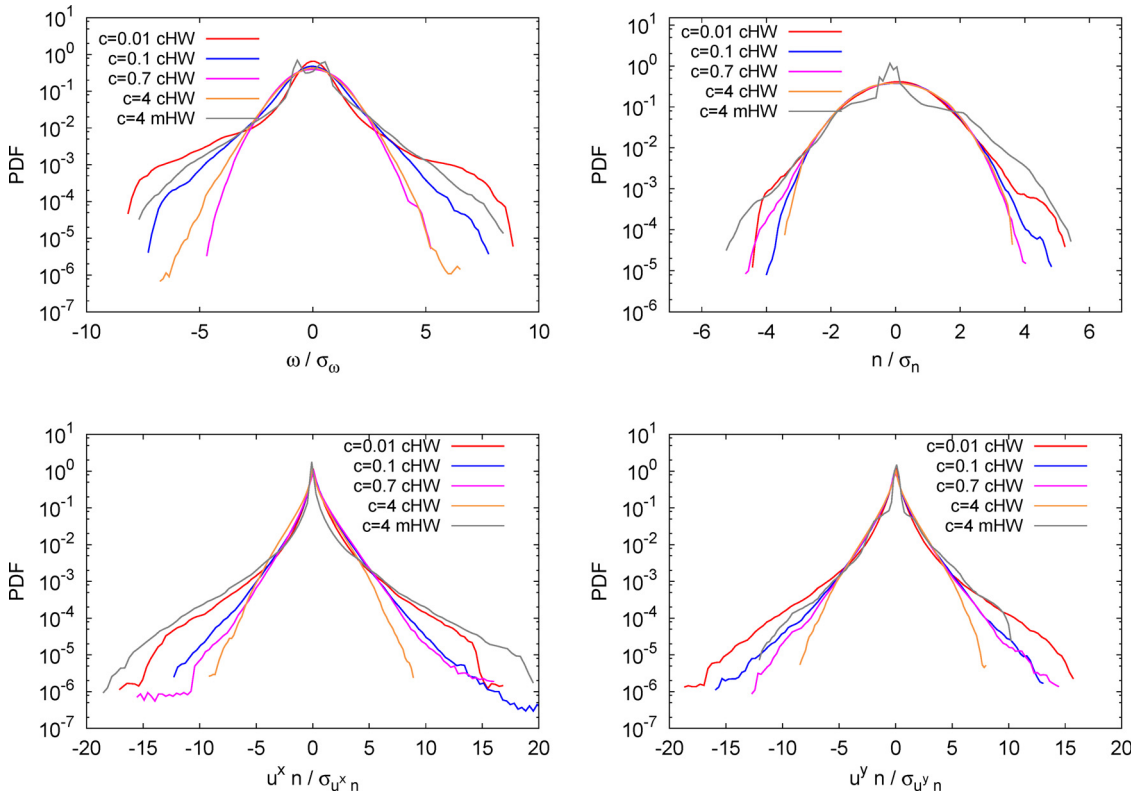

FIG. 4. Top: PDFs (normalized by the corresponding standard deviation) of Eulerian vorticity (left) and density fluctuations (right). Bottom: PDFs (normalized by the corresponding standard deviation) of Eulerian density flux in x and y-directions.

TABLE II. Second order centered moments, M_2, and flatness, F, of different Lagrangian quantities, i.e., the x-component of velocity (u_L^x) and acceleration (a_L^x), Weiss value (Q_L), vorticity (ω_L) and density (n_L) computed from the corresponding PDFs. Only the skewness S of Q_L is shown, since the other quantities yield skewness values close to zero. (The values of the moments for Eulerian quantities are almost the same as for Lagrangian quantities.)

	u_L^x	a_L^x	Q_L	ω_L	n_L	u_L^x	a_L^x	Q_L	ω_L	n_L	Q_L
Configurations			M_2					F			S
$c = 0.01$ cHW	5.0086	28.4189	15.6211	4.2059	182.0711	4.9765	40.6484	86.0252	14.3067	3.3713	−7.1784
$c = 0.05$ *cHW*	4.1107	20.3524	20.5109	6.8190	56.3207	3.7661	32.8554	67.1198	7.7039	3.0216	−5.9186
$c = 0.10$ cHW	3.3151	12.5433	16.4683	7.4005	31.5241	3.4671	28.6267	58.1253	5.5382	2.8321	−5.0000
$c = 0.70$ cHW	2.2778	5.2765	9.1490	8.1136	7.6012	3.2973	8.6850	13.5941	3.0570	2.8147	−1.5099
$c = 2.00$ cHW	1.9671	3.2987	4.2101	5.6229	6.6556	3.4499	6.9236	11.1652	3.0240	2.9646	−1.0842
$c = 4.00$ cHW	1.6056	1.1687	0.7853	2.3188	13.0173	3.4526	6.2109	18.3221	3.4360	2.7814	−1.6767
$c = 2.00$ mHW	0.0046	0.0011	0.0001	0.0636	0.6399	12.2982	18.2834	33.5518	1.8105	2.5214	−2.9332
$c = 4.00$ mHW	0.0148	0.0050	0.0009	0.0621	0.3197	14.3581	28.3987	92.1782	8.2050	4.9547	−4.7475

and become decreasingly important for increasing adiabaticity, which is in agreement with the observations in Ref. 41. Strongly hyperbolic regions are localized in the cells which are surrounding the vortices. We can also note that the dominant structures are circular for low adiabaticity and become thinner and more elongated for large adiabaticity. It reveals also that the strong hyperbolic regions are not concentrated anymore in cells surrounding the vortices for large adiabaticity values. As a consequence, the strong elliptic regions are less localized. Concerning the zonal flows, strong elliptical and hyperbolic regions are located in the ascending regions and exhibit similar large shape, while only intermediate zones are present in the descending regions. Finally, some sample trajectories of three particles for the different configurations are plotted in Fig. 5 (bottom). From $c = 0.01$ cHW to $c = 0.1$ cHW, the trajectories are similar. For increasing c values from 0.7 on for cHW, they are more elongated. For modified HW, the particles exhibit almost straight line trajectories. This is due to the presence of zonal flows which destroy the formation and presence of vortices. The particles are confined in a band with the same velocity along the y-direction, and only "few" particles are able to escape and change zones.

B. Lagrangian statistics

The PDFs of the Lagrangian velocity and acceleration, the latter computed using Eq. (4), shown in Fig. 6, exhibit a change of behavior with c. The corresponding values of the centered second order moments and the flatness are given in Table II. The PDFs of the Lagrangian velocity display Gaussian shape for classical HW, except for large c values where small asymmetries appear in the velocity along the y-direction. The PDFs of the Lagrangian velocity in the modified HW are of a different nature with symmetric heavy tails for the x-direction. The PDFs of Lagrangian acceleration exhibit exponential shape for large adiabaticity values (the flatness values in Table II are close to 6, corresponding to a Laplace distribution) with a smaller width for increasing c, corresponding to reduced variance quantified in Table II, and heavy tails for small c corresponding to large flatness values, which is in agreement with the findings in Ref. 20. For $c = 2$ mHW (results not shown), some asymmetry does appear for the x-direction.

In Fig. 7 (top), we observe that the PDFs of the Lagrangian vorticity and density are almost identical to the PDFs of the corresponding Eulerian quantities shown in Fig. 4. For a statistically stationary flow which is incompressible, it is expected that for advected quantities (here vorticity and density), the Lagrangian particle samples the Eulerian flow domain uniformly due to the volume preserving property of the flow field and, thus, for sufficient long time averages the statistics coincide, assuming ergodicity. The almost perfect agreement between Eulerian and Lagrangian PDFs, thus, confirms that the statistical sampling is sufficient. In the PDFs of the Lagrangian vorticity, it is found, for low adiabaticity values, that asymmetries are present, corresponding to positively skewed PDFs. For the adiabatic regime and $c \geq 2$ (cHW), the PDFs have an almost Gaussian shape. Furthermore, the PDFs of Lagrangian density fluctuations are Gaussian for large adiabaticities. The mean values (not shown) are, as expected, almost equal to zero. In contrast, we can observe strong differences for second order moments and flatness values, as quantified in Table II. We observe that the variance in density decreases with increasing adiabaticity, except for $c = 4$ for which we find a larger value. The flatness values likewise decrease with increasing c, and we can identify a sub-Gaussian behavior with values below 3.

The PDFs of Lagrangian Weiss values, in Fig. 7 (bottom), are negatively skewed, i.e., they show more negative values for low adiabaticities, similar to what was observed in Ref. 41. This is reflected in the presence of more pronounced vortical structures in the flow, as it can be observed in Fig. 5. However, in Ref. 41 the variances are comparable and this is the skewness that best differentiates the hydrodynamic and adiabatic regimes; while in this study, the values of adiabaticity affect the different moments that allow us to characterize the PDFs in Table II. In particular, the variance decreases for larger values of c. This is probably due to a lower Reynolds number in Ref. 41. For increasing adiabaticities, the PDFs become increasingly symmetric, which corresponds to the absence of the vortical structures and, thus, a significant change of flow topology. However, for modified HW, the increase in asymmetry in the PDFs of Lagrangian Weiss values for large c reveals that some vortical structures are formed due to the presence of shear flows, which tend to destabilize and generate Kelvin–Helmholtz vortices. The PDFs of the Weiss values in Fig. 7 nicely illustrate also the large differences in the range of Q. Splitting the flow field into three distinct regions is based on the standard deviation of Q, which is in the mHW much smaller. This means that even if the values of Q are much

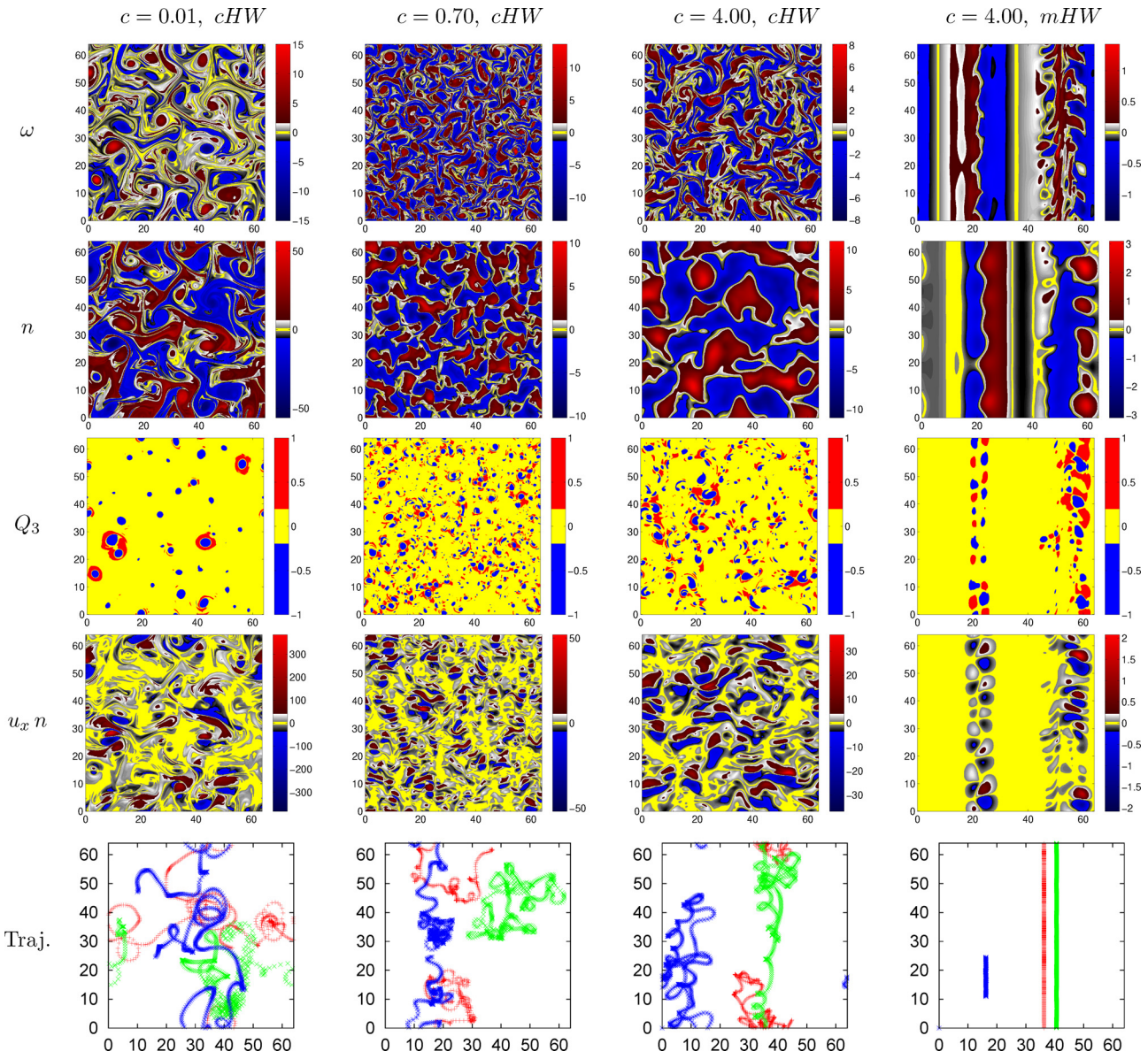

FIG. 5. Flow visualizations for *cHW* with $c = 0.01, 0.7$, and 4.0, and for mHW with $c = 4.0$ (from left to right). From top to bottom: snapshots of vorticity field ω, density fluctuation field n, three-level Weiss field Q_3, density flux in x-direction $u_x\, n$, and three typical tracer trajectories in the statistically stationary regime. Here, Q_3 is the trinary Weiss field with values $-1, 0$, and 1 computed from Q using the threshold Q_0 defined in Sec. II C.

smaller in the case of zonal flows (cf. Table II), we still observe hyperbolic and elliptic regions, as shown in Fig. 5 (right column).

Table II shows the second order moment values and the flatness of the different Lagrangian quantities. The skewness values, which quantify the asymmetry of the PDF, are only given for the Weiss value, as for the other quantities values close to zero are found.

C. Residence times

As it is difficult to adopt an objective definition of a trapping event and the construction of the waiting-time PDF is nontrivial, one possible procedure is to use the PDF of residence times in strongly elliptic regions, to construct the waiting-time distribution. This PDF provides an objective quantitative measure of the time a particle stays on a vortex. Motivated by this approach, which has been applied in Ref. 12 for 2D Navier–Stokes turbulence, we consider, thus, the PDFs of the residence time conditioned with respect to the three-level Lagrangian Weiss value, shown in Fig. 8. These PDFs determine the probability that a given Lagrangian tracer stays in a region with the same value of the three-level normalized Weiss field for a given time τ. Note that Gaussian fluctuations, characteristics of the turbulent

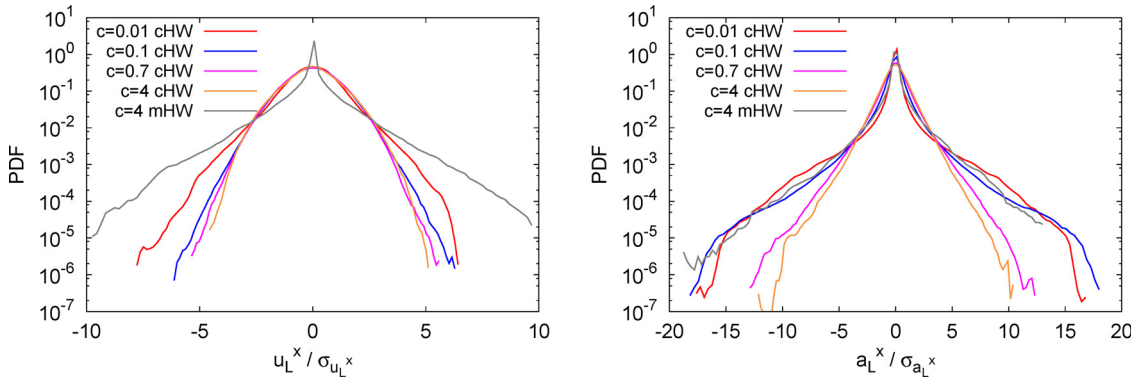

FIG. 6. PDFs (normalized by the corresponding standard deviation) of the *x*-component of Lagrangian velocity (left) and Lagrangian acceleration (right).

background, yield an exponential decay of the residence time PDF. This behavior, observed for 2D Navier–Stokes in Ref. 12, is still present for different flow regimes obtained with the Hasegawa–Wakatani model, that is to say, algebraic tails for strongly hyperbolic and elliptic regions, and exponential decay for intermediate regions, which can be modeled by a Poisson process. The longest residence times are found for intermediate regions. The times are longer for strongly elliptic regions than for strongly hyperbolic regions, which are explained by the particle trapping in elliptic zones. Although similar slopes are obtained for Navier–Stokes and hydrodynamic regimes in the strong elliptic regions, the slopes of the different regions are different for the different regimes, which means that the information of the different dynamics is contained in the value of the slopes for residence time and not in algebraic or exponential behaviors. The difference between the elliptic and hyperbolic regions tends to disappear for the largest *c* value. This is confirmed by the mean and centered second order

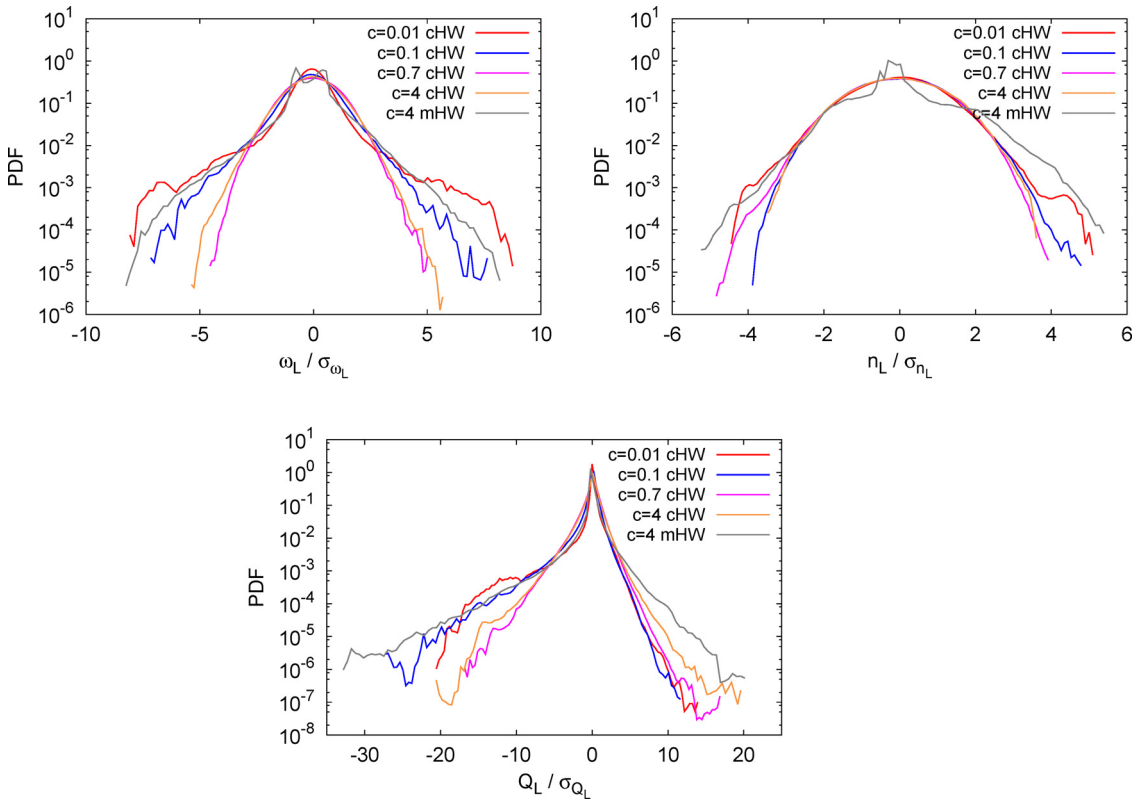

FIG. 7. PDFs (normalized by the corresponding standard deviation) of Lagrangian vorticity (top left), Lagrangian density fluctuations (top right) and Lagrangian Weiss value (bottom center).

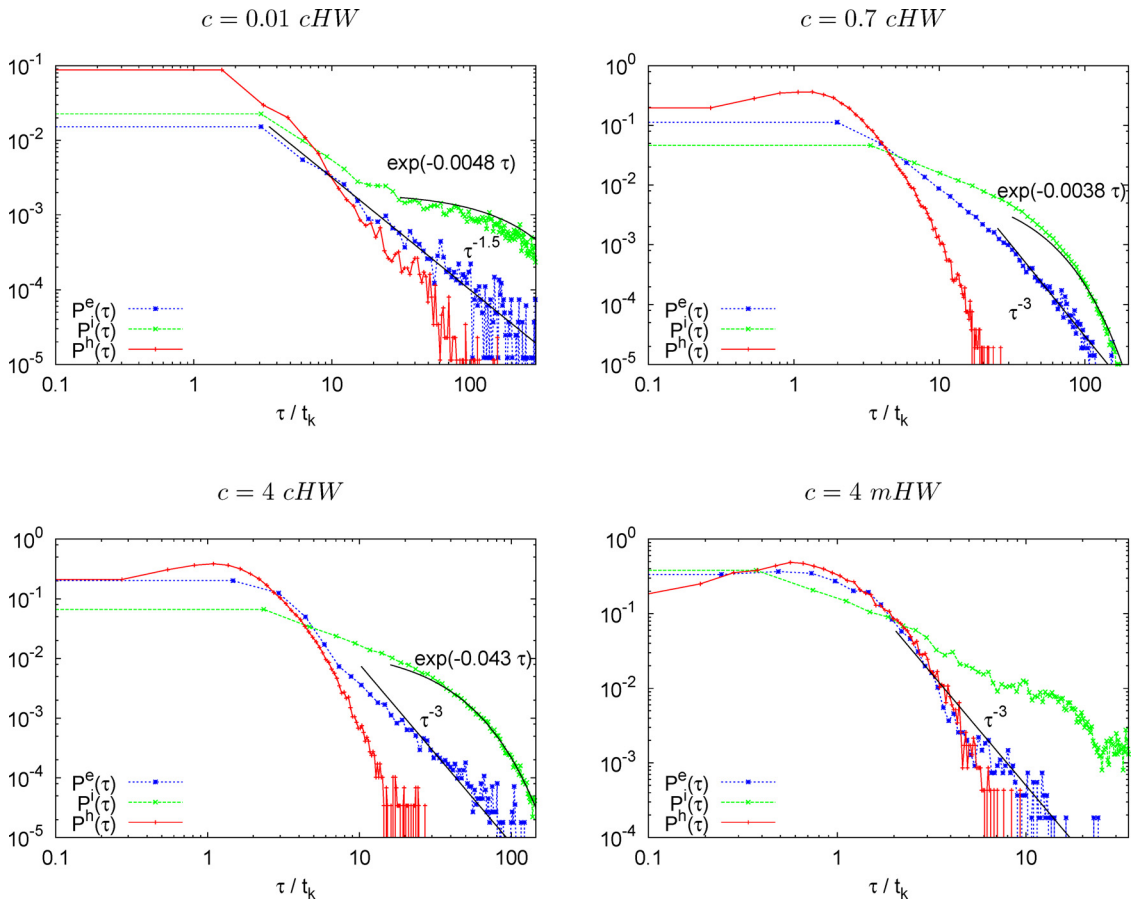

FIG. 8. PDFs (normalized by the mean eddy turn over time) of residence time conditioned with respect to the three-level Lagrangian Weiss value for cHW with $c = 0.01$ (top left), $c = 0.7$ (top right), $c = 4$ (bottom left), and mHW with $c = 4$ (bottom right). The superscripts *e*, *h*, and *i* correspond to elliptic, hyperbolic, and intermediate regions, respectively.

moments shown in Table III. Moreover, we can remark that the strongest mean residence time and centered second order moment are found for intermediate regions, while the weakest values appear for strongly hyperbolic regions. The influence of adiabaticity is weak for strongly elliptic and hyperbolic regions, illustrated by the fact that the exponents do not differ much. For intermediate regions, the adiabaticity has a stronger influence by changing significantly the shape of the PDFs as a function of the adiabaticity. We can note also that the

TABLE III. Mean values, M_1, and centered second order moments, M_2, of the residence time conditioned with respect to the three-level Lagrangian Weiss value in elliptic, hyperbolic, and intermediate flow regions.

	Elliptic	Hyperbolic	Intermediate	Elliptic	Hyperbolic	Intermediate
Configurations		M_1			M_2	
$c = 0.01$ cHW	1.6293	0.6383	18.9589	89.7212	5.1834	1510.6079
$c = 0.05$ cHW	1.3667	0.4343	10.1370	42.7289	1.3205	404.3433
$c = 0.10$ cHW	1.2164	0.4726	7.3025	23.7842	0.6241	196.5689
$c = 0.70$ cHW	1.1092	0.6207	3.5919	7.7833	0.2904	40.5284
$c = 2.00$ cHW	1.1889	0.7495	4.1236	9.0669	0.4016	59.8395
$c = 4.00$ cHW	1.4298	1.0489	6.4262	9.9284	0.8594	126.2423
$c = 2.00$ mHW	3.2256	3.7636	30.5442	19.1787	19.7127	2527.8072
$c = 4.00$ mHW	2.4194	2.5951	36.3946	15.7416	10.5522	3034.8132

behaviors are the same for large adiabaticity $c \geq 0.7$ cHW. Concerning the modified HW case, the residence times are somewhat longer for strongly hyperbolic regions than for elliptic ones, because the shapes of these two zones are of the same nature as confirmed by the visualizations in Fig. 5. We can also note that the behavior of the strongly elliptic and hyperbolic zones is similar for $c = 0.01$ cHW and $c = 4$ mHW despite the qualitatively distinct flow profiles. This may result from the mobility of the flow structures.

D. Conditional Lagrangian statistics

The conditional PDFs are computed from the ensemble average of different Lagrangian quantities for the same region, i.e., elliptic, hyperbolic, and intermediate regions. As a consequence, the integral of each PDF is equal to one.

Figure 9 shows the PDFs of the Lagrangian velocity in the x-direction conditioned with respect to the three-level Weiss value, and Table IV assembles the corresponding moments. First, we find that the intermediate zones dominantly determine the shape of the total PDF. The differences between the zones tend to disappear with increasing adiabaticity for classical HW. Moreover, the differences are much more pronounced for the modified HW case. The behavior of the y-component of the Lagrangian velocity (not shown) is very similar with respect to the contribution of the different zones and their shape. An exception is the modified HW case due to the presence of zonal flows in the y-direction.

The PDFs of Lagrangian acceleration in the x-direction conditioned with respect to the three-level Weiss value and the corresponding moments are given in Fig. 10 and Table V, respectively. The intermediate zones yield the largest contribution to the total PDF; however, the contributions from elliptic and hyperbolic regions are not negligible. Similarly as for the Lagrangian velocities, the differences between the zones are less pronounced with increasing adiabaticity for classical HW, and the discrepancies are more significant for modified HW. The same trend for the contribution of the different zones is observed for the y-component of the Lagrangian acceleration (not shown here).

Figure 11 shows the PDFs of curvature again conditioned with respect to the three-level Weiss value. We can see that they are very similar to the ones obtained for hydrodynamics shown in Ref. 12. For small adiabaticity, the PDFs decay algebraically with an exponent somewhat stronger than −2, which demonstrates the presence of

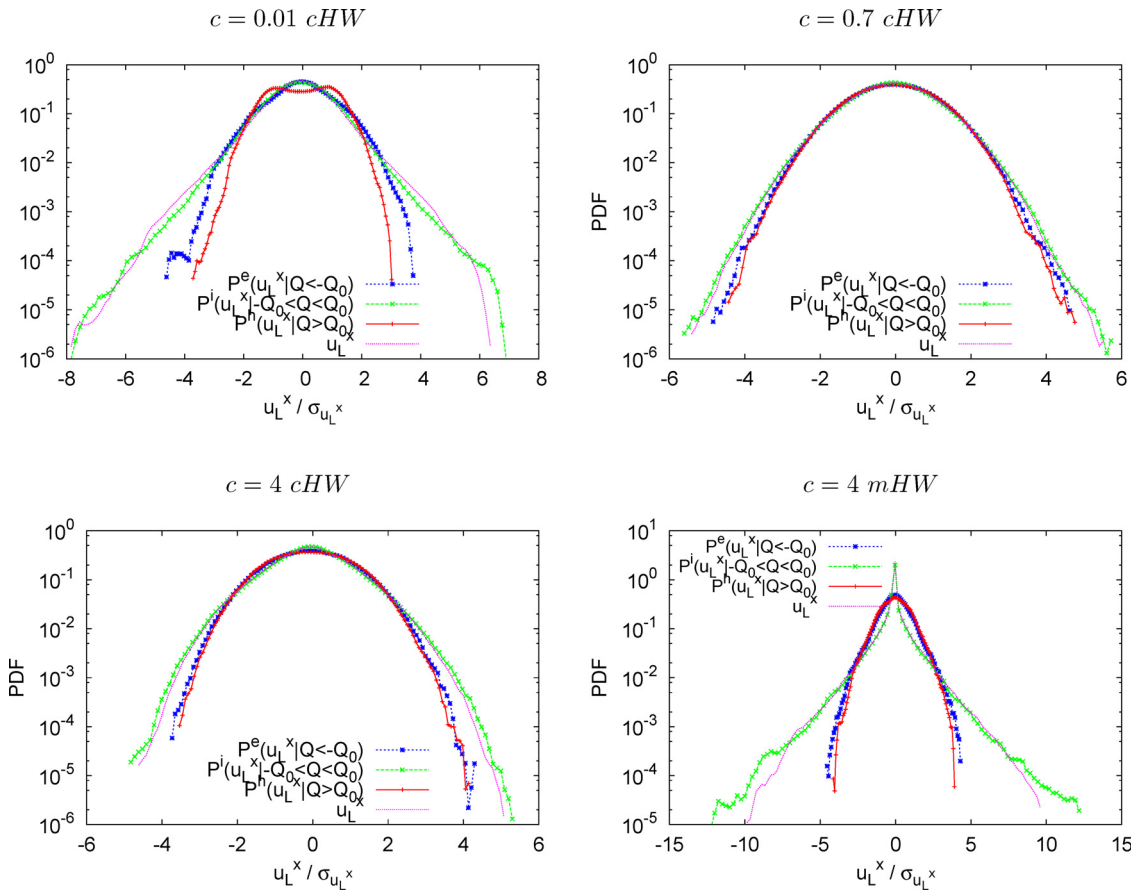

FIG. 9. PDFs (normalized by the corresponding standard deviation) of Lagrangian conditional x-component velocity with respect to the three-level Lagrangian Weiss value for cHW with $c = 0.01$ (top left), $c = 0.7$ (top right), $c = 4$ (bottom left), and mHW with $c = 4$ (bottom right). The superscripts e, h, and i correspond to elliptic, hyperbolic, and intermediate regions, respectively.

TABLE IV. Centered second order moments M_2 of the Lagrangian conditional velocity in the x-direction with respect to three level Weiss value.

Configurations	Total	Elliptic	Hyperbolic	Intermediate
$c = 0.01$ cHW	5.0086	14.4400	22.1881	4.0210
$c = 0.05$ cHW	4.1107	7.3493	11.1180	3.6194
$c = 0.10$ cHW	3.3151	4.9838	6.6300	3.0151
$c = 0.70$ cHW	2.2778	2.8150	3.0719	2.1254
$c = 2.00$ cHW	1.9671	2.5252	2.7331	1.8108
$c = 4.00$ cHW	1.6056	2.1397	2.3951	1.4678
$c = 2.00$ mHW	0.0046	0.0162	0.0176	0.0028
$c = 4.00$ mHW	0.0148	0.0679	0.0820	0.0092

intermittency in these regimes. For large adiabaticity, the decay exponent is precisely -2, which is exactly the exponent we predict from Gaussian PDFs of the Lagrangian velocity in two-dimensions. This can be explained by the fact that $1/u^2$ yields an inverse chi-square distribution. As a consequence, the decay exponent of the PDF of $1/u^2$ is -2.[42] The PDF of curvature is, therefore, an additional tool to quantify the presence of Lagrangian intermittency. From this latter point, we can conclude that the hydrodynamic regime is slightly intermittent. The regimes then become decreasingly intermittent for increasing adiabaticity since the deviation from the decay exponent −2 becomes less and less important. Furthermore, for the different regimes, we can claim that the intermediate regions are not intermittent from a Lagrangian point of view.

Motivated by Ref. 5 where the authors studied the radial flux of plasma density, we analyze the density gradients in the different flow regions.

The PDFs of density gradients in the radial direction, $\partial n/\partial x$, conditioned with respect to the three-level Weiss value and its corresponding moments are shown in Fig. 12 and Table VI for two cases, $c = 0.7$ and 4 for cHW. The PDFs in the poloidal direction, $\partial n/\partial y$ are not shown as their shape is similar. For the adiabatic regime (cHW with $c = 0.7$), we find exponential tails for the total flow and the flow conditioned with the three level Weiss values. The deformation dominated regions yield the largest variance, while for intermediate and vortical regions similar values as in the PDF of the total flow can be observed. In contrast in the geostrophic regime (cHW with $c = 4$), all density gradient PDFs are Gaussian-like and, thus, have a parabola

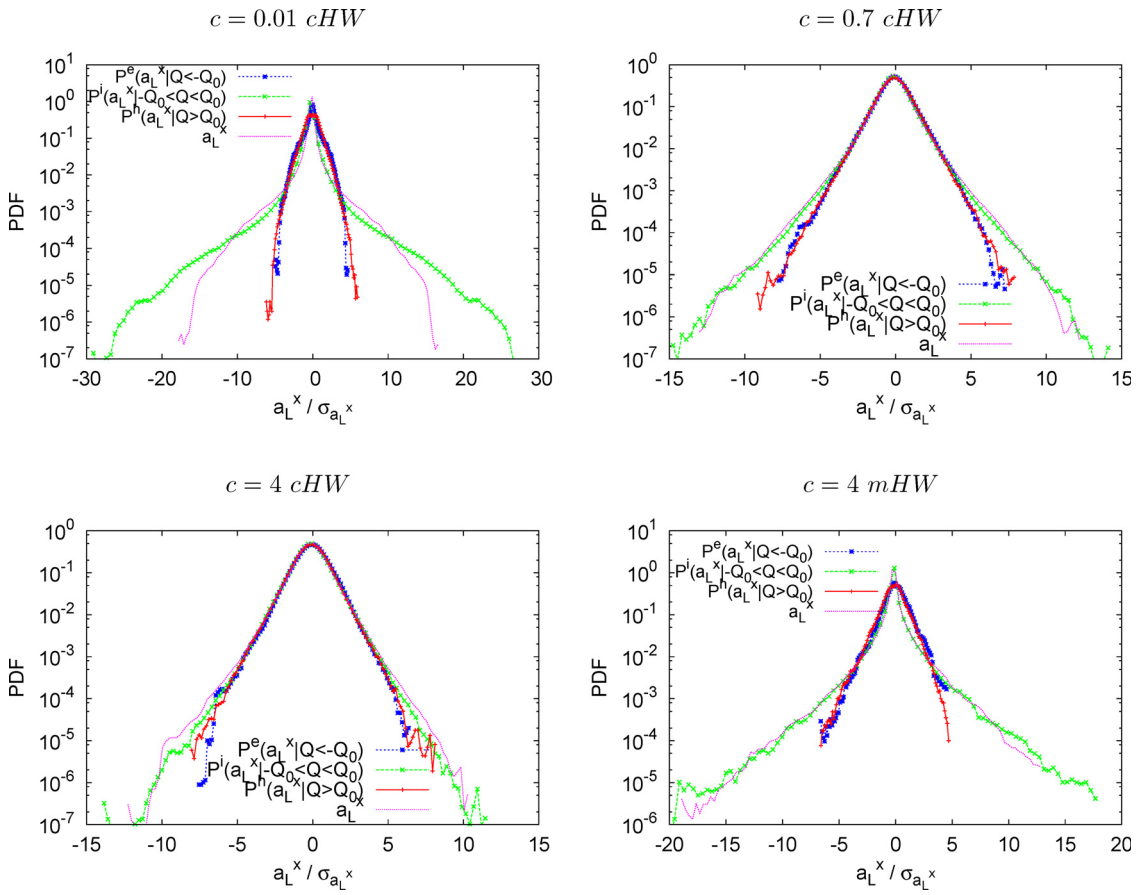

FIG. 10. PDFs (normalized by the corresponding standard deviation) of Lagrangian conditional x-component acceleration with respect to the three-level Lagrangian Weiss value for cHW with $c = 0.01$ (top left), $c = 0.7$ (top right), $c = 4$ (bottom left), and mHW with $c = 4$ (bottom right). The superscripts e, h, and i correspond to elliptic, hyperbolic, and intermediate regions, respectively.

TABLE V. Centered second order moments M_2 of the Lagrangian conditional acceleration in the x-direction with respect to three level Weiss values.

Configurations	Total	Elliptic	Hyperbolic	Intermediate
$c = 0.01$ cHW	28.4189	365.0659	202.4553	9.4091
$c = 0.05$ cHW	20.3524	159.6248	100.1495	8.8480
$c = 0.10$ cHW	12.5433	74.1288	45.5502	6.3184
$c = 0.70$ cHW	5.2765	14.8643	9.8476	3.5906
$c = 2.00$ cHW	3.2987	8.2545	5.6727	2.3909
$c = 4.00$ cHW	1.1687	2.7853	1.8783	0.9165
$c = 2.00$ mHW	0.0011	0.0062	0.0044	0.0004
$c = 4.00$ mHW	0.0050	0.0400	0.0277	0.0023

shape. Their variances are similar too. For the hydrodynamic regime (cHW with $c = 0.01$, not shown here), we observe heavy tails of the density gradients in both directions for negative Weiss values, i.e., vorticity dominated regions. In the intermediate regions, we find exponential tails, similar to the PDFs of the total field. For the deformation dominated regions, the variance is strongly reduced. Finally, for mHW (results not shown here), the zonal flows have a pronounced signature in the density gradient PDFs in the radial direction, while in the poloidal direction exponential tails can be seen. These results are consistent with Ref. 5, since exponential tails correspond to non-Gaussian characteristics of the turbulent fluctuations, and the radial flux of plasma density behaves similar to Bohm diffusion.

E. Mean curvature angle

The directional change of tracer particles is analyzed by considering the curvature angle, as defined in Eq. (7) and the coarse-grained curvature at different scales, introduced in Sec. II B. Figure 13 (left) shows the mean curvature angle, $\theta(\tau) \equiv \langle|\Theta(t,\tau)|\rangle$, where $\langle\cdot\rangle$ denotes the ensemble and time average as a function of the time increments for different adiabaticity values. The mean angles increase monotonically from 0 to $\pi/2$. This means that particles have for small τ the tendency going straight, similar to what was found in Ref. 13, while for very large τ their motion becomes uncorrelated and they have the same probability traveling in any direction. This results in a mean angle of $\pi/2$, as we are taking the absolute value and do not distinguish between left and right turns. For all regimes, i.e., cHW and mHW, we identify for small τ a clear linear scaling behavior $\propto \tau$,

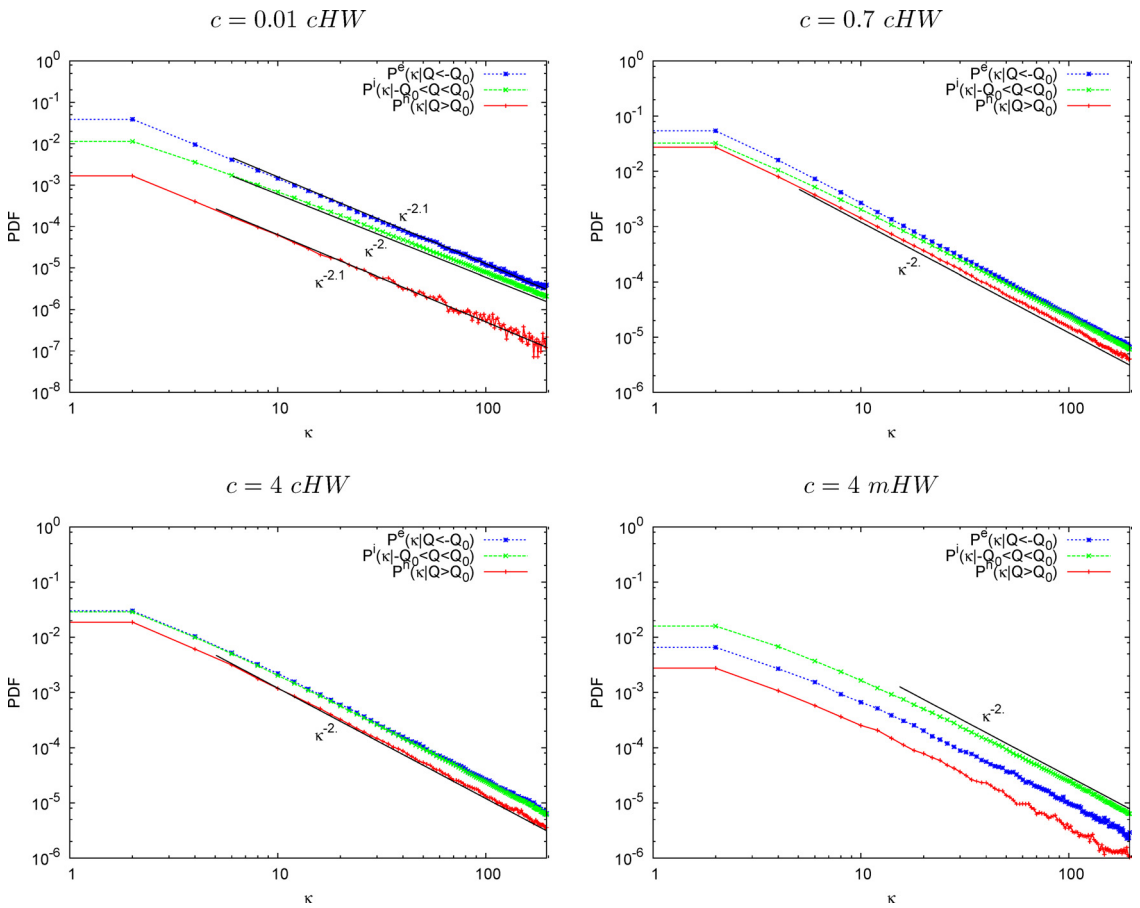

FIG. 11. PDFs of Lagrangian conditional curvature κ with respect to the three-level Lagrangian Weiss value for cHW with $c = 0.01$ (top left), $c = 0.7$ (top right), $c = 4$ (bottom left), and mHW with $c = 4$ (bottom right).

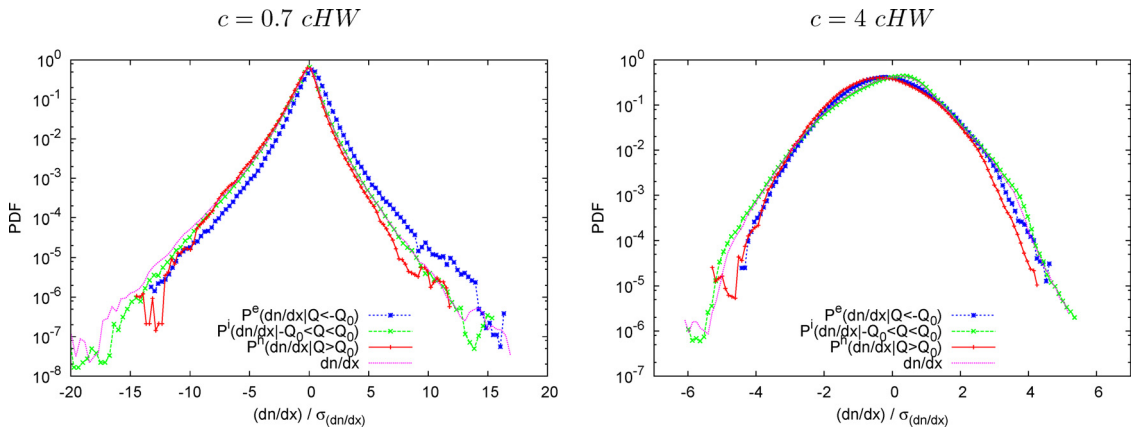

FIG. 12. PDFs (normalized by the corresponding standard deviation) of Lagrangian conditional density gradient in the *x*-direction with respect to three level Weiss value for cHW with $c = 0.7$ (left) and $c = 4$ (right). The superscripts *e*, *h*, and *i* correspond to elliptic, hyperbolic, and intermediate regions, respectively.

TABLE VI. Centered second order moments M_2 of the Lagrangian conditional density gradient in the *x*-direction with respect to three level Weiss values.

Configurations	Total	Elliptic	Hyperbolic	Intermediate
$c = 0.01$ cHW	369.9536	86.5196	500.4799	374.6142
$c = 0.05$ cHW	150.2175	33.3487	264.3132	151.8040
$c = 0.10$ cHW	79.6720	19.2353	166.9093	79.1641
$c = 0.70$ cHW	6.6706	4.3437	13.5971	6.0811
$c = 2.00$ cHW	2.1487	2.6816	3.0584	1.9588
$c = 4.00$ cHW	1.4374	1.7607	1.9080	1.3386
$c = 2.00$ mHW	0.0629	0.0850	0.0550	0.0539
$c = 4.00$ mHW	0.0466	0.1284	0.1051	0.0376

followed by a transition without a clearly observed powerlaw scaling of $\tau^{1/2}$. This so-called inertial scaling that we would except at least in the case $c = 0.01$ cHW is absent and probably only visible in much larger resolution computations. A change of the curvature occurs for $\tau \sim t_k$ in the classical cases and much later for the modified cases. This is in agreement for cHW with Ref. 13 since different behaviors are predicted theoretically in Navier–Stokes for $\tau \ll t_k$, for intermediate values of τ and for large τ. In Fig. 13 (right), the zoom illustrates for large τ that for $c > 0.01$ the mean angle is slightly larger than $\pi/2$. Concerning the modified case, where zonal flows are present, the multi-scale curvature is radically diminished at all time-lags, reflecting the reduced radial motion of the fluid particles and the anisotropy of the flow structure. We can also note that for mHW the behavior at large τ is different. Instead of presenting an asymptotic value for $c = 2$ and 4 for the mHW model, the mean angles decrease similarly to what is found for flows in porous media.[43] One possible explanation for the asymptotic behavior for the largest τ is that the value reflects the proportion of particles that change the flow region.

Figure 14 (left) shows the mean coarse-grained curvature angle $\kappa_c(\tau)$ with $\kappa_c(\tau) \equiv \langle |K(t,\tau)| \rangle$, where $K(t,\tau) = \Theta(\tau)/(2\tau||\boldsymbol{u}||)$ and $\langle \cdot \rangle$ denotes the ensemble and time average as a function of the time increments for different adiabaticity values. We find that the mean curvatures decrease monotonically from values of $0.5 - 1.8$ to 6×10^{-3}, when τ increases. For all regimes and for $\tau/t_k < 1$, the coarse-grained curvature exhibits an algebraic scaling behavior which should tend to a constant $1/(2||\boldsymbol{u}(t)||)$ when $\tau \to 0$ because $\Theta(t, \tau \to 0) \sim \tau$. For large τ, the same algebraic scaling behavior $\propto \tau^{-1}$ is observed in all cases, as expected, since $\Theta(t, \tau \to \infty) \sim \pi/2$. In Fig. 14 (right), the zoom at large τ illustrates that the slope of the mean coarse-grained

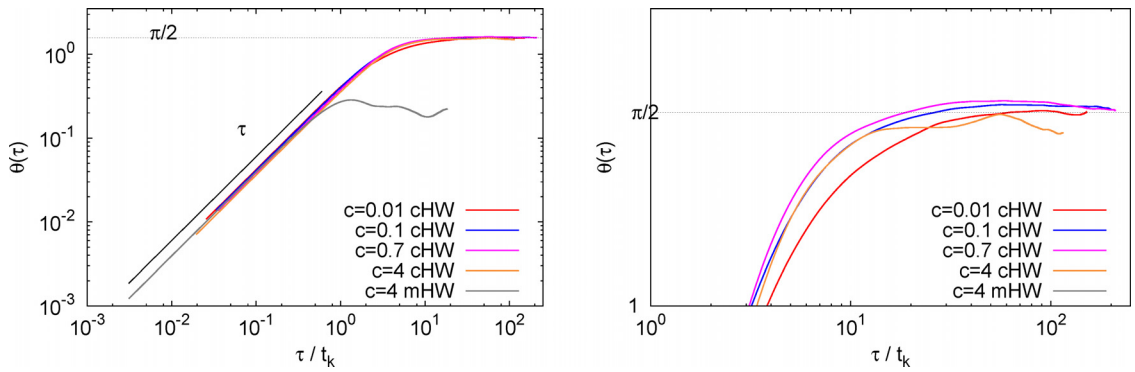

FIG. 13. Mean curvature angle $\theta(\tau)$ as a function of τ/t_k for the different flow regimes. A corresponding zoom for large increments τ/t_k is shown on the right.

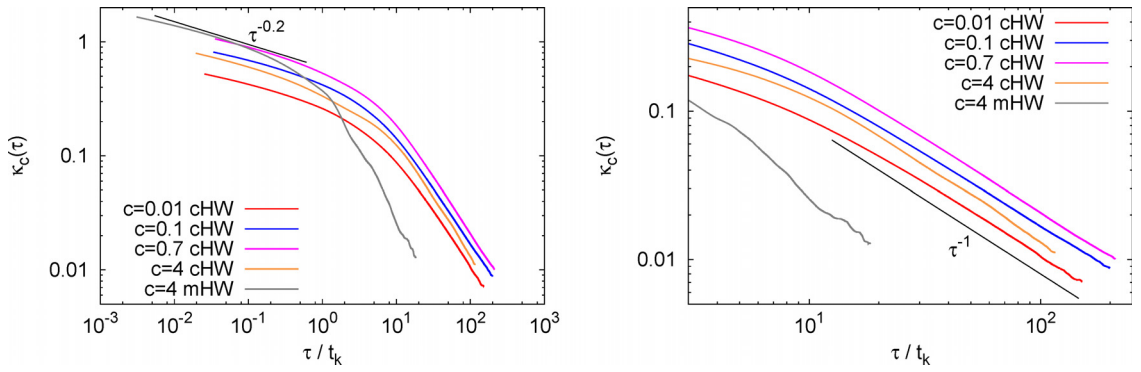

FIG. 14. Mean coarse-grained curvature $\kappa_c(\tau)$ as a function of τ/t_k for the different flow regimes. A corresponding zoom for large τ/t_k ($20 < \tau/\tau_k < 250$) is shown on the right.

curvature angle is the same for different adiabaticity values c in the case of cHW. In contrast for mHW with $c = 2$ and 4 mHW, we find instead of a pronounced τ^{-1} scaling that $\kappa_c(\tau)$ fluctuates, which is probably due to the presence of zonal flows.

IV. CONCLUSIONS

We performed extensive numerical studies for a wide parameter range of the classical Hasegawa–Wakatani model and its modified version governing the plasma flow and the observed electrostatic drift-wave turbulence in the tokamak edge. The modified Hasegawa–Wakatani model allows us to assess the influence of zonal flows. In the proposed Lagrangian approach, different statistics were performed for ensembles of tracers along their trajectories. Conditional averages using the Okubo–Weiss criterion were computed, and the flow topology was decomposed into different regions, vertical, or deformation dominated and intermediate regions. The influence of the adiabaticity parameter c, which is related to the parallel dynamics of the plasma and the nonlinear cascades in the parallel direction, has been investigated in a systematic way, including the quasi adiabatic regime of relevance to edge plasma turbulence. Moreover, we also performed simulations for values beyond the ones relevant for describing plasma edge turbulence to explore a large parameter space. We also studied the adiabatic limit ($c \gg 1$) for which the model reduces to a Hasegawa–Mima type equation, i.e., the geostrophic flows and the limit $c \ll 1$ for which we recover a Navier–Stokes system, i.e., hydrodynamic flows. Furthermore, motivated by the fact that in the classical system the turbulent flow remains isotropic for low values of the adiabaticity parameter and zonal flows are absent, we performed simulations for a modified Hasegawa–Wakatani system.

The Eulerian and Lagrangian statistics allowed us to characterize the unalike complex dynamics of the flows and the tracer transport, as mentioned above.

Analyzing the co-spectrum of velocity and density fluctuations in the radial direction yields insight into the contributions of the density flux at different length scales. Indeed, the co-spectrum decomposes the total flux into scale-wise contributions, and thus, we can quantify the strength of the flux for different wavenumbers k. For details, we refer to Refs. 34 and 44 and the cited references therein. The observed inertial scaling of $k^{-7/2}$ is found to be in good agreement with predictions based on dimensional arguments.

Another important result is that the behavior of the residence time, observed in two-dimensional homogeneous isotropic turbulence,[12] is still valid for the different Hasegawa–Wakatani regimes. The influence of vortex trapping, which explains the longest residence times in strong elliptic regions, tends to disappear with increasing adiabaticity and the residence times from strong elliptic and hyperbolic regions become of the same order. Moreover, the presence of zonal flows that induces shear flows, for modified HW, implies a slightly larger contribution from strong hyperbolic regions compared to strong elliptical ones. Furthermore, the conditional Lagrangian statistics with respect to three level Weiss values reveal that the intermediate zones are responsible for the total PDF, and the differences between the different zones are reduced with increasing adiabaticity for classical HW. However, again due to the presence of shear flows, the contributions of intermediate zones are still of major importance for modified HW. Indeed, the strong elliptic and hyperbolic regions are located in the zone where shear flows appear.

An analysis of radial density gradients shows that PDFs have exponential tails in the cHW quasi-adiabatic regime. These results are in agreement with Ref. 5 where the authors showed that turbulence fluctuations have non-Gaussian characteristics, while the radial flux of plasma density is similar to Bohm diffusion.

Directional statistics considering the angular change of the Lagrangian tracer particles reveal a multiscale measure for the coarse grained curvature. We, thus, quantified the directional properties of the complex particle motion at different time scales for the different flow regimes.

In forthcoming work, multiscale angular Lagrangian statistics can be considered to characterize the directional change of inertial particles and their clustering, e.g., related to impurities in the plasma, at different time scales and show the significance of zonal flows for transport.

ACKNOWLEDGMENTS

D.C.N. acknowledges support from the Oak Ridge National Laboratory, managed by UT-Battelle, LLC, for the U.S. Department of Energy under Contract No. DE-AC05–00OR22725. D.C.N. also gratefully acknowledges the support and hospitality of the École Centrale de Marseille for the visiting positions during the elaboration of this work. K.S. acknowledges partial support by the French

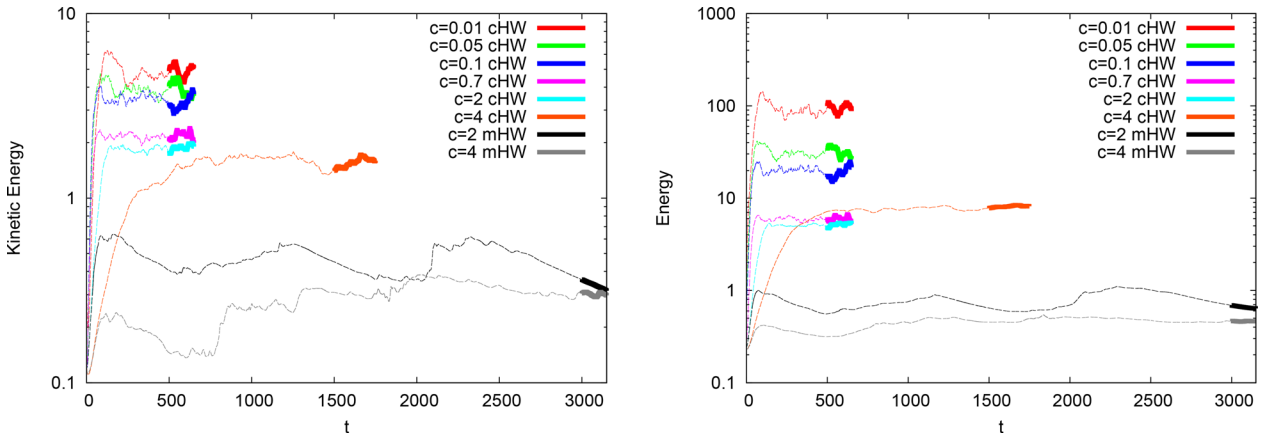

FIG. 15. Time evolution of kinetic energy $E_{kin} = 0.5\langle u^2 \rangle$ (left) and total energy $E_{tot} = E_{kin} + 0.5\langle n^2 \rangle$ (right). The thickened part of the lines indicates the time interval where the statistics of the particle trajectories are performed: From $t = 500$ to $t = 650$ for cHW with $c = 0.01, 0.05, 0.1, 0.7$, and 2. From $t = 1000$ to $t = 1150$ for cHW with $c = 4$. From $t = 3000$ to $t = 3150$ for mHW with $c = 2$ and $c = 4$.

Federation for Magnetic Fusion Studies (FR-FCM) and the Eurofusion consortium, funded by the Euratom Research and Training Programme 2014–2018, 2019–2020, and 2021–2022 under Grant Agreement No. 633053. The views and opinions expressed herein do not necessarily reflect those of the European Commission. Centre de Calcul Intensif d'Aix-Marseille is acknowledged for granting access to its high performance computing resources. K.S. thanks Professor Pat Diamond and the Organizers of the Festival de Théorie in Aix-en-Provence, France for discussions, which triggered some of the presented investigations on the modified Hasegawa–Wakatani system.

AUTHOR DECLARATIONS

Conflict of Interest

The authors have no conflicts to disclose.

Author Contributions

Benjamin Kadoch: Writing – original draft (equal); Writing – review & editing (equal). **Diego del-Castillo-Negrete:** Writing – original draft (equal); Writing – review & editing (equal). **Wouter J. T. Bos:** Writing – original draft (equal); Writing – review & editing (equal). **Kai Schneider:** Writing – original draft (equal); Writing – review & editing (equal).

DATA AVAILABILITY

The data that support the findings of this study are available from the corresponding author upon reasonable request.

APPENDIX: FLOW DYNAMICS

To get insight into the flow dynamics, the time evolution of kinetic energy $E_{kin} = 0.5\langle u^2 \rangle$ and total energy $E_{tot} = E_{kin} + 0.5\langle n^2 \rangle$ are shown in Fig. 15. After some transition time, exhibiting drift-wave instabilities, all configurations reach a statistically steady state, even if some fluctuations in the energy are still present. In the cHW case, the fluctuations are more important for $c = 4$ than for $c = 2$. The thickened part of the lines corresponds to the time interval, about 150 mean eddy turn over times in all cases, where the statistics of the particle trajectories have been performed.

REFERENCES

[1]S. I. Krasheninnikov, D. A. D'Ippolito, and J. R. Myra, "Recent theoretical progress in understanding coherent structures in edge and SOL turbulence," J. Plasma Phys. **74**, 679–717 (2008).
[2]D. del Castillo-Negrete, B. A. Carreras, and V. E. Lynch, "Fractional diffusion in plasma turbulence," Phys. Plasmas **11**, 3854–3864 (2004).
[3]B. P. van Milligen, R. Sánchez, and B. A. Carreras, "Probabilistic finite-size transport models for fusion: Anomalous transport and scaling laws," Phys. Plasmas **11**, 2272–2285 (2004).
[4]D. del Castillo-Negrete, "Asymmetric transport and non-Gaussian statistics of passive scalars in vortices in shear," Phys. Fluids **10**, 576–594 (1998).
[5]M. V. Umansky, P. Popovich, T. A. Carter, B. Friedman, and W. M. Nevins, "Numerical simulation and analysis of plasma turbulence the large plasma device," Phys. Plasmas **18**, 055709 (2011).
[6]S. Garland, K. Reuther, M. Ramisch, and P. Manz, "The collisionality dependence of intermittency level in drift-wave turbulence in the stellarator TJ-K," Phys. Plasmas **24**, 112307 (2017).
[7]S. Garland, P. Manz, and M. Ramisch, "The influence of magnetic field curvature on intermittency in drift-wave turbulence in the stellarator TJ-K," Phys. Plasmas **27**, 052304 (2020).
[8]R. Metzler and J. Klafter, "Accelerating Brownian motion: A fractional dynamics approach to fast diffusion," Europhys. Lett. **51**, 492–498 (2000).
[9]J. A. Mier, R. Sánchez, L. García, D. E. Newman, and B. A. Carreras, "On the nature of transport in near-critical dissipative-trapped-electron-mode turbulence: Effect of a subdominant diffusive channel," Phys. Plasmas **15**, 112301 (2008).
[10]B. A. Carreras, V. E. Lynch, and G. M. Zaslavsky, "Anomalous diffusion and exit time distribution of particle tracers in plasma turbulence model," Phys. Plasmas **8**, 5096–5103 (2001).
[11]L. García and B. A. Carreras, "Mesoscale transport properties induced by near critical resistive pressure-gradient-driven turbulence in toroidal geometry," Phys. Plasmas **13**, 022310 (2006).
[12]B. Kadoch, D. del Castillo-Negrete, W. J. T. Bos, and K. Schneider, "Lagrangian statistics and flow topology in forced two-dimensional turbulence," Phys. Rev. E **83**, 036314 (2011).
[13]W. J. T. Bos, B. Kadoch, and K. Schneider, "Angular statistics of Lagrangian trajectories in turbulence," Phys. Rev. Lett. **114**, 214502 (2015).

[14]T. Stoltzfus-Dueck, B. D. Scott, and J. A. Krommes, "Nonadiabatic electron response in the Hasegawa-Wakatani equations," Phys. Plasmas **20**, 082314 (2013).
[15]W. Horton and Y.-H. Ichikawa, *Chaos and Structures in Nonlinear Plasmas* (World Scientific, 1996).
[16]R. Numata, R. Ball, and R. L. Dewar, "Bifurcation in electrostatic resistive drift wave turbulence," Phys. Plasmas **14**, 102312 (2007).
[17]A. V. Pushkarev, W. J. T. Bos, and S. V. Nazarenko, "Zonal flow generation and its feedback on turbulence production in drift wave turbulence," Phys. Plasmas **20**, 042304 (2013).
[18]E. Lévêque and A. Naso, "Introduction of longitudinal and transverse Lagrangian velocity increments in homogeneous and isotropic turbulence," Europhys. Lett. **108**, 54004 (2014).
[19]A. Hasegawa and M. Wakatani, "Plasma edge turbulence," Phys. Rev. Lett. **50**, 682–686 (1983).
[20]W. J. T. Bos, B. Kadoch, S. Neffaa, and K. Schneider, "Lagrangian dynamics of drift-wave turbulence," Physica D **239**, 1269–1277 (2010).
[21]S. Futatani, W. J. T. Bos, D. del Castillo-Negrete, K. Schneider, S. Benkadda, and M. Farge, "Coherent vorticity extraction in resistive drift-wave turbulence: Comparison of orthogonal wavelets versus proper orthogonal decomposition," C. R. Phys. **12**, 123–131 (2011).
[22]A. Hasegawa and K. Mima, "Stationary spectrum of strong turbulence in magnetized nonuniform plasma," Phys. Rev. Lett. **39**, 205 (1977).
[23]B. Kadoch, W. J. T. Bos, and K. Schneider, "Extreme Lagrangian acceleration in confined turbulent flow," Phys. Rev. Lett. **100**, 184503 (2008).
[24]S. Burov, S. M. A. Tabei, T. Huynh, M. P. Murrell, L. H. Philipson, S. A. Rice, M. L. Gardel, N. F. Scherer, and A. R. Dinner, "Distribution of directional change as a signature of complex dynamics," Proc. Natl. Acad. Sci. U. S. A. **110**, 19689–19694 (2013).
[25]B. Kadoch, W. J. T. Bos, and K. Schneider, "Directional change of fluid particles in two-dimensional turbulence and of football players," Phys. Rev. Fluids **2**, 064604 (2017).
[26]B. Kadoch, M. Bassenne, M. Esmaily-Moghadam, K. Schneider, M. Farge, and W. J. T. Bos, "Multi-scale geometrical Lagrangian statistics: Extensions and applications to particle-laden turbulent flows," in *Center for Turbulence Research, Proceedings of the Summer Program* (Stanford University, 2016), pp. 53–62.
[27]A. Okubo, "Horizontal dispersion of floatable particles in the vicinity of velocity singularities such as convergences," Deep Sea Res. Oceanog. Abstr. **17**, 445–454 (1970).
[28]J. Weiss, "The dynamics of enstrophy transfer in two-dimensional hydrodynamics," Physica D **48**, 273–294 (1991).
[29]C. Basdevant and T. Philipovitch, "On the validity of the 'Weiss criterion' in two-dimensional turbulence," Physica D **73**, 17–30 (1994).
[30]D. Biskamp, S. J. Camargo, and B. D. Scott, "Spectral properties and statistics of resistive drift-wave turbulence," Phys. Lett. A **186**, 239–244 (1994).
[31]X. Q. Xu and R. H. Cohen, "Scrape-off layer turbulence theory and simulations," Contrib. Plasma Phys. **38**, 158–170 (1998).
[32]J. Lumley, "Similarity and the turbulent energy spectrum," Phys. Fluids **10**, 855–858 (1967).
[33]P. O'Gorman and D. Pullin, "Effect of Schmidt number on the velocity–scalar cospectrum in isotropic turbulence with a mean scalar gradient," J. Fluid Mech. **532**, 111–140 (2005).
[34]W. J. T. Bos, B. Kadoch, K. Schneider, and J.-P. Bertoglio, "Inertial range scaling of the scalar flux spectrum in two-dimensional turbulence," Phys. Fluids **21**, 115105 (2009).
[35]R. Schiestel and B. E. Launder, *Modélisation et Simulation des Écoulements Turbulents* (Traité Des Nouvelles Technologies, 1993).
[36]W. J. T. Bos and J.-P. Bertoglio, "A single-time two-point closure based on fluid particle displacements," Phys. Fluids **18**, 031706 (2006).
[37]R. H. Kraichnan, "Inertial-range transfer in two- and three-dimensional turbulence," J. Fluid Mech. **47**, 525–535 (1971).
[38]S. Nazarenko and J.-P. Laval, "Non-local two-dimensional turbulence and Batchelor's regime for passive scalars," J. Fluid Mech. **408**, 301–321 (2000).
[39]J.-P. Laval, B. Dubrulle, and S. Nazarenko, "Nonlocality and intermittency in three-dimensional turbulence," Phys. Fluids **13**, 1995–2012 (2001).
[40]K. Smith, G. Boccaletti, C. Henning, I. Marinov, C. Tam, I. Held, and G. Vallis, "Turbulent diffusion in the geostrophic inverse cascade," J. Fluid Mech. **469**, 13–48 (2002).
[41]W. J. T. Bos, S. Futatani, S. Benkadda, M. Farge, and K. Schneider, "The role of coherent vorticity in turbulent transport in resistive drift-wave turbulence," Phys. Plasmas **15**, 072305 (2008).
[42]H. Xu, N. T. Ouellette, and E. Bodenschatz, "Curvature of Lagrangian trajectories in turbulence," Phys. Rev. Lett. **98**, 050201 (2007).
[43]X. He, S. Apte, K. Schneider, and B. Kadoch, "Angular multiscale statistics of turbulence in a porous bed," Phys. Rev. Fluids **3**, 084501 (2018).
[44]P. O'Gorman, "Theory and simulation of passive scalar mixing in the presence of a mean scalar gradient," Ph.D. thesis (California Institute of Technology, 2004).